UNIVERSITÀ DEGLI STUDI DI MILANO

FACOLTÀ DI SCIENZE E TECNOLOGIE

CORSO DI LAUREA MAGISTRALE IN FISICA

A feasibility study of an innovative imaging technique for range monitoring in Particle Therapy

Relatore:

Prof. Cristina LENARDI

Correlatore:

Dott. Ilaria MATTEI

Candidato:

Giacomo CALVI

Matricola:

919131

Anno Accademico 2018 - 2019

Contents

Introduction **1**

1 Particle Therapy **4**
1.1 Charged heavy particles . . . 6
1.1.1 Range . . . 8
1.1.2 Bragg Peak . . . 10
1.1.3 Multiple Coulomb scattering . . . 10
1.1.4 Nuclear fragmentation . . . 11
1.2 Radiobiology . . . 13
1.2.1 Linear Energy Transfer . . . 13
1.2.2 DNA damage . . . 14
1.2.3 Relative Biological Effectiveness . . . 14
1.2.4 RBE and biological processes . . . 16
1.3 Facilities and treatment . . . 16
1.3.1 Facilities . . . 17
1.3.2 Treatment planning . . . 18

2 Range Monitoring **19**
2.1 Range uncertainties . . . 20
2.2 Range monitoring techniques . . . 21
2.2.1 PET-gamma . . . 21
2.2.2 Prompt gamma . . . 22
2.2.3 Charged particles . . . 27
2.3 Research and development . . . 28

3 The PAPRICA chamber **29**
3.1 PAPRICA physics . . . 31
3.1.1 Photon interactions . . . 31
3.1.2 Pair production . . . 31
3.1.3 Electron and positron interactions . . . 34
3.2 Detectors . . . 35

3.2.1 Converter . . . 35
3.2.2 Tracker . . . 36
3.2.3 Calorimeter . . . 37
3.3 Reconstruction algorithm . . . 38
3.3.1 Vertex calculation . . . 38
3.3.2 Photon momentum . . . 39
3.3.3 Photon emission point . . . 40

4 Events dynamic **43**
4.1 Monte Carlo simulations . . . 43
4.1.1 The FLUKA code . . . 43
4.1.2 PAPRICA simulations . . . 44
4.2 Converter efficiency . . . 46
4.2.1 Pair production efficiency . . . 46
4.2.2 Crossing efficiency . . . 46
4.3 Angular resolution . . . 47
4.3.1 Pair Production . . . 47
4.3.2 Converter crossing . . . 49
4.3.3 Tracker crossing . . . 50
4.4 Signal properties . . . 52

5 Chamber optimization **53**
5.1 Real case scenario . . . 53
5.2 Vertex reconstruction . . . 54
5.3 Converter optimization . . . 55
5.3.1 Efficiency . . . 55
5.3.2 Resolution . . . 56
5.4 Tracker optimization . . . 58
5.4.1 Efficiency . . . 59
5.4.2 Resolution . . . 59
5.4.3 Photon energy selection . . . 60
5.5 Calorimeter geometry . . . 61
5.6 Final design . . . 62

6 Prompt gamma reconstruction **63**
6.1 Identification of tracks . . . 64
6.1.1 Chi-squared test . . . 65
6.1.2 Track selection . . . 65
6.2 Backtracking . . . 67
6.2.1 Energy measurement . . . 67

6.2.2 Lepton momentum estimate 69
6.3 Results 70

Conclusions **72**

A FLUKA output **74**

Bibliography **80**

Introduction

According to the World Health Organisation (WHO), cancer is the second leading cause of death in the world [1]. Today, three therapies are mainly used for the treatment of tumors: surgery, in which the tumor is directly removed from the body, chemotherapy, a type of treatment based on drug administration, and radiotherapy, a clinical practice that uses ionizing radiation, in particular photons, in order to damage the DNA of diseased cells. A kind of treatment, or more often a combination of them, is chosen according to the tumour biological properties and localisation in the human body. Particle Therapy (PT) is an innovative radiotherapy technique for cancer treatment in which the dose deposition inside the patient body is made by heavy charged particles (protons or heavier ions). Recently, in Italy and other EU countries, PT was inserted in the essential levels of assistance, demonstrating that this therapy is now well recognised as an effective and competitive tool for tumour control. The development of particle therapy has been driven by the search for a technique that minimizes the radiation administered to healthy tissues during the cancer treatment. The energy release mechanism of charged particles, governed by the interactions with the nuclei electrons, results in the well-known Bragg Peak (BP) distribution: as the particle slows down, the energy release increases, peaking near the particle stopping position. The BP extension is of the order of millimeters, while the size of tumors is of the order of centimeters. By changing the particle energy, it is possible to treat the whole target volume. The use of PT to treat deep seated tumors reduces significantly, with respect to conventional radiotherapy, the dose release to the healthy tissues surrounding the tumour.

The spatial selectivity of the energy release requires high accuracy in predicting the particle range, however, several factors may lead to a wrong range estimation, resulting in a shift of the Bragg peak position and to an under-dosage of the tumour volume. Although several methods have been developed to correctly estimate the position of the range and reduce uncertainties, a larger volume is irradiated during the treatment, providing safety margins to ensure complete coverage of the tumor. A great effort has been made in the last years to develop an on-line range and dose monitoring system for PT applications, in order to reduce the safety margins of the treatment. Range monitoring systems are based on the detection of secondary radiation produced by the interaction between charged

particle beam and biological tissue nuclei. This radiation is in fact correlated in energy, space and time with the primary beam range. The PAPRICA project, started in 2019 by a collaboration between the Istituto Nazionale di Fisica Nucleare (INFN) and the Università Sapienza di Roma, proposes an innovative method for range monitoring, exploiting the prompt gamma pair production mechanism. The measurement of four-momentum of the pair makes it possible to reconstruct the incident photon direction and subsequently the spatial distribution of the emitted gamma rays. The subject of this thesis is the feasibility study, through Monte Carlo simulations, of the PAPRICA imaging technique.

In Chapter 1 a brief review of the particle therapy is proposed, discussing the interaction mechanisms between radiation and tissues both from physical and biological point of view. The last section of this chapter summarizes the main characteristic of PT facilities and modalities of treatment.

Chapter 2 reports the state of the art of range monitoring techniques, discussing the main prompt gamma imaging methods with the relative advantages and limits.

Chapter 3 focuses on the design of the PAPRICA chamber. The different detectors that compose it and the algorithm to reconstruct the photon direction are illustrated.

Chapter 4 introduces the fundamental quantities in the study and optimization of the PAPRICA performance.

In Chapter 5 the optimization of the PAPRICA geometry is described. In particular, the chapter focuses on the material choice of the converter layer and on the optimization of the tracker and calorimeter geometry.

Chapter 6 presents the experimental-like reconstruction method with goal to recognize the particle tracks and associate the correct momentum to each of them, leading to photon reconstruction.

Chapter 1

Particle Therapy

The idea of using radiation for medical applications was born as soon as X-rays were discovered by Wilhelm Röntgen in 1895. In the following decades, various imaging techniques and therapies were developed thanks to the properties of radiation. The harmful effect on biological tissue, consisting of DNA damage that prevents cell reproduction, suggested the application of ionizing radiation in the treatment of cancer. The physical quantity that measures the delivered radiation is the dose, defined as the energy release by radiation per unit mass:

$$D = \frac{dE}{dm} \tag{1.1}$$

The goal of radiation therapy is to release a radiation dose into the tumor volume, in order to kill the diseased cells, avoiding at the same time the exposure of healthy ones. The dose released in healthy tissues may lead, in fact, to the appearance of side effects, that can occur months or years after the therapy administration, including a large set of pathologies depending on the cancer type, i.e. fibrosis, infertility or a second cancer caused by radiation exposure. The calculation of the dose value a tumor should be irradiated with is always a trade-off between cancer treatment and side effects due to the exposure of healthy tissue (see Figure 1.1). The choice of therapy to treat the tumour varies according to the type and location of the tumour itself and usually several therapies, with and without radiation, are carried out simultaneously to achieve the best result in tumour containment. Nowadays, the conventional radiotherapy is based on X and gamma rays, that are characterized by a high penetration power. There are two techniques for administering the dose: brachytherapy, or internal radiotherapy, involving the positioning of a radiation source inside or next to the tumor volume and external beam radiotherapy, that administers the radiation dose by means of an external photon beam. The cutting-edge technology actually available in external conventional radiotherapy is the Intensity-Modulated Radiation Therapy (IMRT), in which six up to nine non co-planar photon beams are used to build up a highly compliant dose distribution over the tumour.

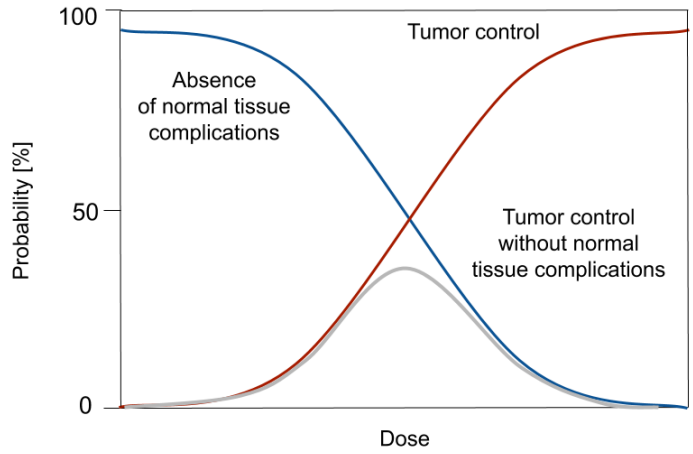

Figure 1.1: Probability of tumor control and normal tissue complications as a function of the dose, adapted from [2].

In 1946 Robert Wilson proposed to use charged particles, as protons or light ions, for radiation therapy treatments [3]. The main advantage of Particle Therapy (PT), also called hadrontherapy, is the high spatial selectivity of dose distribution, with a maximum dose (Bragg peak) released close to the point where the particles stop (see Figure 1.2). This property allows to deliver the radiation with high accuracy to the tumor, reducing healthy tissue exposure. The development and diffusion of PT have become possible in recent decades thanks to the considerable progress in the field of particle accelerators. Nowadays, particle therapy is a well-known technique for tumor treatment and it is mainly based on proton beams with an energy range between 50 and 250 MeV, and carbon ion (^{12}C) beams, with energy between 80 and 400 MeV/u.

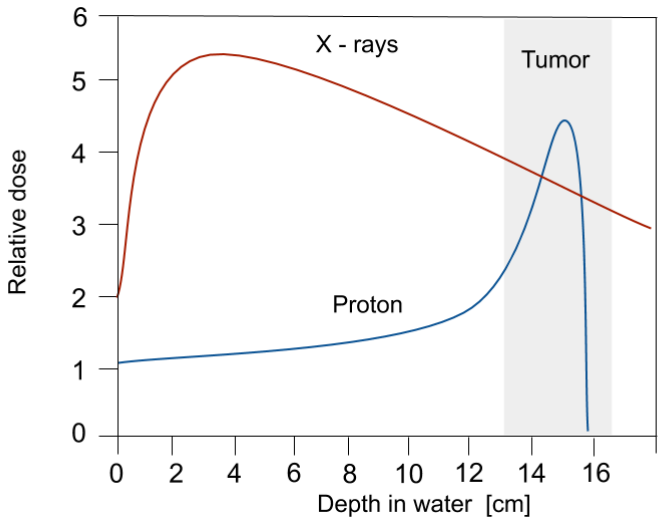

Figure 1.2: Dose release in water as a function of depth for photon (red) and 148 MeV proton beam (blue), adapted from [2]. The dose spatial distribution of charged particle is characterized by the Bragg peak.

More than 130 000 patients were treated with particle therapy worldwide from 1954 to 2014, 86% of which were treated with protons and 14% with carbon ions or with other particles [4]. As of December 2019, there are over 90 particle therapy facilities, and at least 35 others under construction, each with one or more treatment rooms [5][6].
The purpose of this chapter is to provide a brief review of the interactions of charged particles with matter and their effects on biological tissues. A description of PT facilities and treatment modalities will be presented in the last section.

1.1 Charged heavy particles

The interaction between radiation and matter strongly depends on type, charge and mass of radiation. For charged heavy particles, that include all particles with the mass many times greater than electron mass, as protons, ions, muons etc. the interaction with matter is driven by Coulomb interaction with electrons of the medium. At the energies of interest for particle therapy, the emission of bremsstrahlung radiation is negligible and, due to the high electron density, Coulomb and nuclear interactions with nuclei are secondary processes. In each electronic interaction, a charged particle transfers only a small fraction of its kinetic energy and a large number of impacts are required to slow it down. The incident radiation interacts simultaneously with many electrons and consequently suffers a continuous energy loss. The medium electron can be promoted to a higher shell (excitation) or be completely removed from the atom (ionization). In rare cases the transferred energy could be enough to generate delta rays, electrons which can travel far away from the impact point and become source of other ionisation processes. The stopping power, defined as the energy loss per unit path length, describes the charge particle dynamics in a medium:

$$S = -\frac{dE}{dx} \tag{1.2}$$

A first expression of the stopping power was given by Bohr, using classic mechanics, but the correct quantum calculation was performed by Bethe and Bloch [7]:

$$-\frac{dE}{dx} = 2\pi \frac{N_a Z \rho}{A} \frac{r_e^2 m_e c^2 Z_p^2}{\beta^2} \left(\ln \frac{2 m_e c^2 \beta^2 \gamma^2 W_{max}}{I^2} - 2\beta^2 - \delta(\gamma) - 2\frac{C}{Z} \right) \tag{1.3}$$

The parameter I is the mean excitation potential that represents the average excitation energy of the electrons in the medium and has a key role in the stopping power formula. It is a very difficult parameter to estimate with theoretical calculations and for this reason is often derived from experimental stopping power measurements. The physical quantity W_{max} is the maximum energy transfer per interaction and may be deduced from kinematic

calculations

$$W_{max} = \frac{2m_e c^2 \beta^2 \gamma^2}{1 + 2\frac{m_e}{M}\sqrt{1+\beta^2\gamma^2} + \frac{m_e^2}{M^2}} \tag{1.4}$$

The term δ takes into account the effect of electron polarisation, called density effect, that shields far electrons and reduces the stopping power. The parameter C, called shell correction, describes the variations of the stopping power when the incident particle speed is comparable or lower than the orbital speed of the bound electrons. The other physical quantities are shown in Table 1.1.

N_a	Avogadro constant
Z	Atomic number of absorbing material
A	Atomic weight of absorbing material
ρ	Density of absorbing material
r_e	Classical electron radius
m_e	Electron mass
c	Light speed
Z_p	Charge of projectile (in units of e)
β	v/c of projectile
γ	Lorentz factor

Table 1.1: Physical quantities present in Equation 1.3.

The dependence of the Bethe formula on the particle speed is described by the factor $1/\beta^2$. With increasing speed, the stopping power decreases to a minimum point, called minimum ionization point, beyond which, it increases again due to the logarithmic factor (see Figure 1.3). The energy loss depends linearly on the square of the particle charge: particles with a higher charge undergo a faster energy loss (see Figure 1.4).

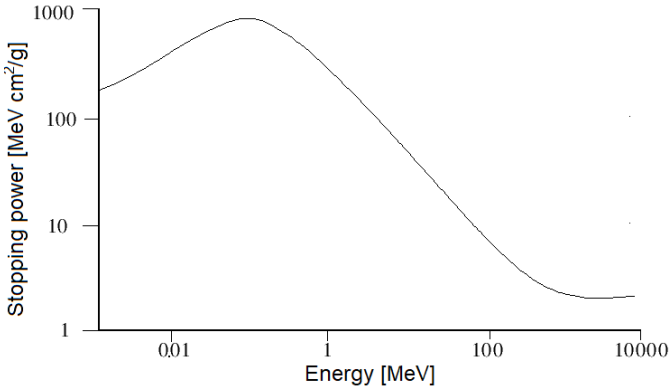

Figure 1.3: Trend of the proton stopping power as a function of particle energy [8].

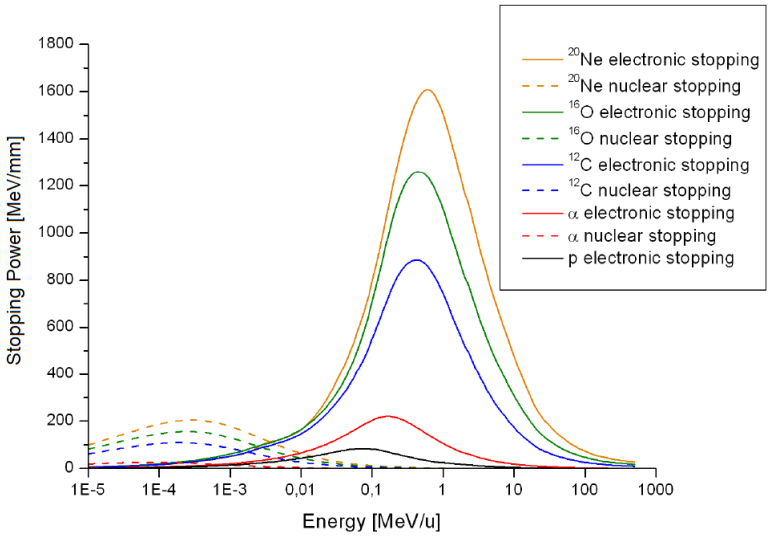

Figure 1.4: Comparison between the stopping power of different charged particles in water, calculated with a simulation code [9]. The contribution of nuclear interactions is also reported with a dotted line.

1.1.1 Range

The range is defined as the depth reached by a particle beam in a medium. The number of interactions and the energy release are not the same for each particle and vary according to the individual trajectory, resulting in different ranges. This effect is known as range straggling. The range value can be therefore statistically described by a probability function. For large traversed thicknesses, the range dispersion is described by a Gauss distribution, centered in the average range R with a relative standard deviation equal to [10]:

$$\frac{\sigma_R}{R} = \frac{1}{\sqrt{Mc^2}} f\left(\frac{E_0}{M}\right) \tag{1.5}$$

f is a function that varies slowly depending on the absorber, M is the particle mass and E_0 the initial particle energy. The range can be estimated experimentally by sending a mono-energetic beam to targets of different thicknesses and measuring the fraction of escaped particles. If the thickness is small, all particles can pass through the target. If the thickness is close to the range, the observed fraction of particles decreases rapidly to zero (see Figure 1.5). The average range can be measured as the midpoint of the descent curve, i.e. the point where the fraction of the transmitted particles is equal to 0.5. In many applications it is interesting to know the thickness within which all the particles are absorbed. This thickness, called extrapolated range, can be obtained tracing the straight line tangent to the curve of the transmitted particles versus the absorber thickness and taking the intersection with the X-axis.

The theoretical range can be calculated from the stopping power as:

$$R = \int_0^R dx = \int_0^{E_0} S(E)^{-1} dE \tag{1.6}$$

Figure 1.6 shows the charged particle range in water as a function of the initial energy. The ratio between the range of two heavy charged particles with the same energy per nucleon follows the scaling law, which can be deduced from Equation 1.6 [7] [10]:

$$\frac{R_1}{R_2} = \frac{M_1}{M_2} \frac{z_2^2}{z_1^2} \tag{1.7}$$

Comparing proton and carbon ions the scale factor is equal to 3. Consequently, ion therapy requires higher energy beam to reach deep target.

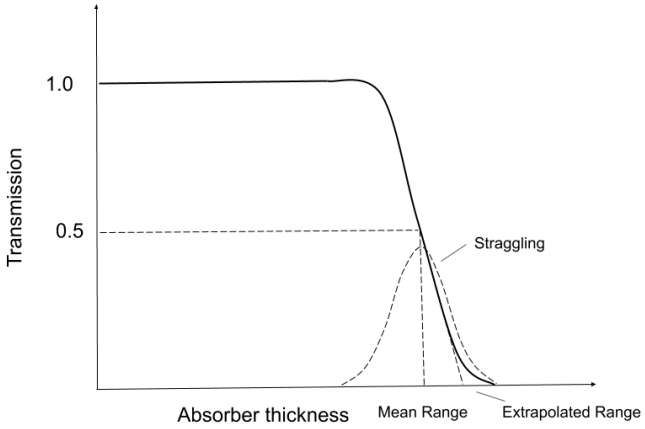

Figure 1.5: Fraction of particles detected in a transmission experiment as a function of the absorber thickness [7].

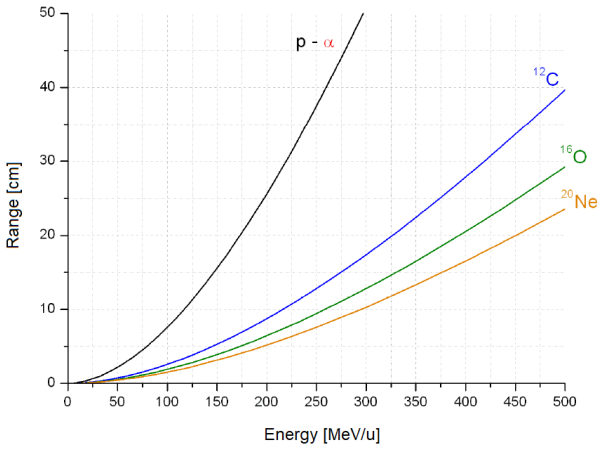

Figure 1.6: Charged particle range in water as a function of the initial energy, obtained with a simulation code [9].

1.1.2 Bragg Peak

The energy loss distribution of a charged particle per unit path length, as a function of the material depth, is called Bragg curve (see Figure 1.7). At high speed the stopping power is dominated by the factor $1/\beta^2$, and the Bragg curve is almost uniform. With increasing depth, the particle slows down and, according to Equation 1.3, the energy loss increases. At the end of the trajectory, the charge of the particle is neutralized by the electronic capture and the stopping power collapses, resulting in a peak, commonly known as Bragg peak (BP). The sharp curve of dose distribution is the charge particle feature that allows a high accuracy in releasing the energy on a deep target. In particle therapy, different beam energies are needed to obtain different particle ranges and build the Spread-Out Bragg Peak (SOBP), in order to have a uniform dose coverage of the extended tumor volume to be treated.

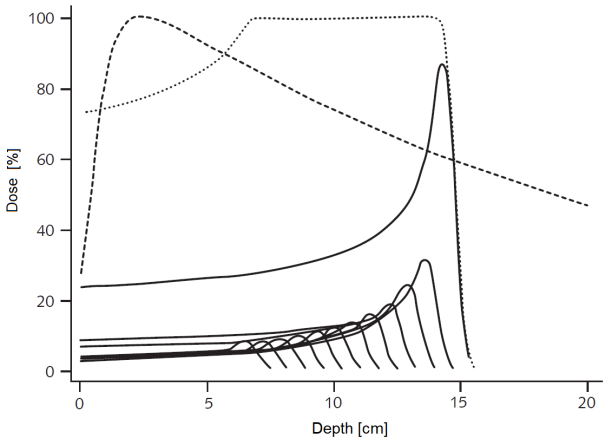

Figure 1.7: Bragg curves for beams of different energies (continuous line) and the spread-out Bragg peak (dotted line). The photon curve is also shown (dashed line) [11].

1.1.3 Multiple Coulomb scattering

The Coulomb and nuclear interactions between the charged particles and the nuclei of the medium are a secondary, but not negligible, process. The main effect on a charged particle beam is the widening of the transversal beam distribution due to multiple scattering. The beam widening depends on the traversed thickness, the medium crossed, the properties of the particles and the beam energy. When the thickness is extremely small and the probability to have more than one interaction is negligible, the effect is well described by the Rutherford formula of the differential cross section [7]:

$$-\frac{d\sigma}{d\Omega} = Z_p^2 Z_t^2 r_e^2 \frac{(m_e c/\beta p)^2}{4\sin^4\left(\frac{\theta}{2}\right)} \tag{1.8}$$

Z_p and Z_t are respectively the atomic number of the particle and the target, p is the momentum of the incident particle and θ is the scattering angle with respect to the beam direction. When the thickness increases and the number of interactions becomes high, the angular dispersion with respect to the beam direction can be modelled as a Gauss distribution, centred in $\theta = 0$, with root mean square [10]:

$$\theta_0 = \frac{14.1MeV}{\beta cp} Z_p \sqrt{\frac{x}{X_0}} \left[1 + \frac{1}{9}\log_{10}(\frac{x}{X_0})\right] \tag{1.9}$$

x is the distance covered in the target and X_0 is the radiation length of the material. Equation 1.9 results in a larger transverse widening for protons with respect to carbon ions. In particle therapy, the beam widening is not a negligible factor and can vary from a few hundreds of micrometers to several millimeters (see Figure 1.8).

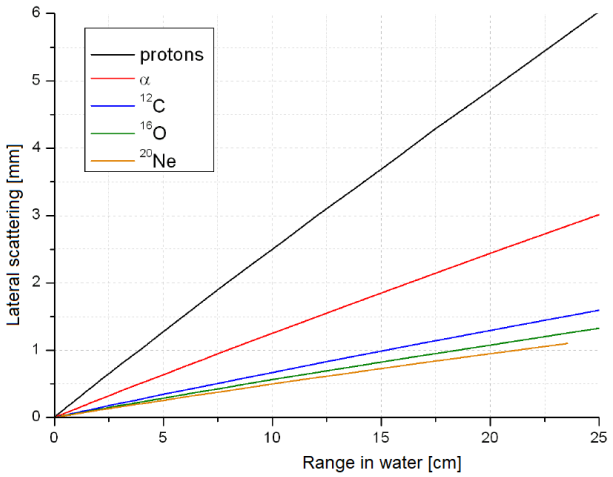

Figure 1.8: Charged particle beam widening in water for different particle beam as a function of range, obtained through a Monte Carlo simulation [9].

1.1.4 Nuclear fragmentation

In particle therapy the energy of protons and light ions may be sufficient to overcome the Coulomb repulsion, leading to a nuclear reaction between the projectile and the target nucleus. Nuclear interactions lead to a fragmentation of the nuclei involved, resulting in the production of secondary particles such as neutrons, protons, hydrogen isotopes or light ions. In the case of proton beams, only target fragmentation can occur. With light ion beams, both target and projectile fragmentation are present and projectile fragments may travel beyond the Bragg peak, forming a tail in the dose (see Figure 1.9). This effect increases with ion beam mass and prevents the use of particles heavier than ^{16}O, unsuitable for PT treatments.

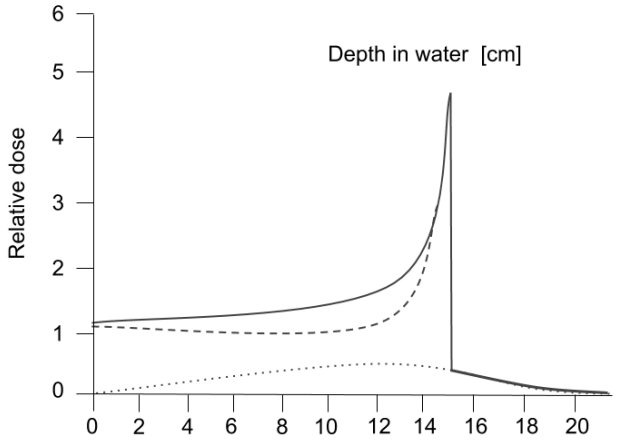

Figure 1.9: Simulation of fragmentation tail in dose spatial distribution of 270 MeV/u carbon ions, adapted from [12]. The solid line is the total calculated Bragg curve, the dashed and dotted lines are respectively the contributions from the primary particles and from secondary fragments.

The nuclear reactions between the beam and the target nuclei, at the energies of particle therapy, can be described using the abrasion-ablation model, represented in Figure 1.10. In the first phase of this model (abrasion) the projectile and the target overlap leading to the interaction between the respective nucleons. This phase is very fast and the interaction takes place on a time scale of $10^{-23} - 10^{-21}$ s. In the second step (ablation) there is a dispersion, called evaporation, of the nucleons involved in the interaction and a de-excitation of the projectile and target fragments. The de-excitation may occur by evaporation of neutrons, protons or light nuclei as well as by fission and emission of gamma rays, with a characteristic time between 10^{-21} and 10^{-16} s.

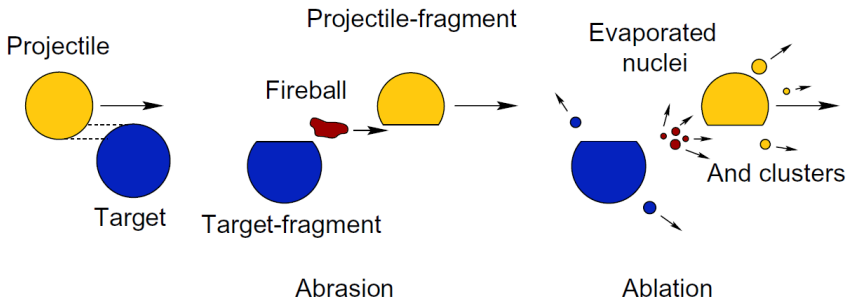

Figure 1.10: Abrasion-ablation model [13].

1.2 Radiobiology

In this section the fundamental quantities of radiobiology, such as LET or RBE, and their correlation with radiation damage to DNA are described. The types of damage that DNA can suffer are many and the accurate treatment of this subject exceeds the purpose of this thesis. However, a brief discussion of this topic will allow to understand why different types of radiation have different effects on biological tissues.

1.2.1 Linear Energy Transfer

As will be presented in the next section, the damage suffered by cells due to radiation is highly dependent on the spatial density of ionization events. The Linear Energy Transfer (LET) is defined as the energy absorbed by the medium in electronic interactions per unit of distance travelled by the radiation:

$$LET_{\Delta} = -\frac{dE_{\Delta}}{dx} \tag{1.10}$$

The linear energy transfer does not take into account high-energy secondary particles, as delta rays, which move away from the main track. The Δ subscript in Equation 1.10 represents the energy limit of the secondary particles considered. The linear energy transfer can be therefore interpreted as the local energy release in the medium, measured in KeV/μm, and is an important quantity in the study of the biological effects of radiation. The ionization density increases with the atomic number of the charged particle (see Figure 1.11), resulting in a higher LET for light ions than for protons.

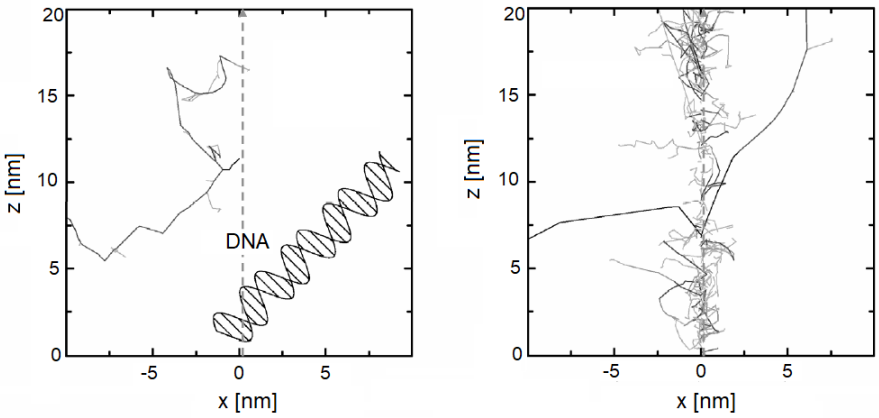

Figure 1.11: The structure of a proton (left) and a carbon (right) track are compared with a schematic representation of a DNA molecule [14].

1.2.2 DNA damage

The harmful effects of ionising radiation on biological tissues are due to damage caused to DNA that prevents cell reproduction. DNA damage can arise directly from the interaction with radiation or indirectly from the interaction with other molecules (in particular water). In the latter case the interaction of radiation with cell molecules produces free radicals that are able to diffuse far enough to reach and chemically damage the DNA. Direct damage is the main mechanism of radiations characterized by a high linear energy transfer, as charged particles. For low-LET radiation, as X-rays, the damage is indirectly inflicted by free-radicals. The physics of the process, i.e. the initial ionization, occurs in 10^{-15} s while the life time of the radicals is of the order of 10^{-9} s. The breaking of the chemical bond in the DNA occurs in 10^{-5} s and the biological effects can occur hours, days, months or years later. In Figure 1.12 a sketch of the DNA and of possible DNA damage is presented. The most common radiation-induced effects are: a single strand break, which can be easily repaired by the cell itself, and the double strand break, where both filaments of the double helix are cut, and repair mechanisms are more difficult to occur [15].

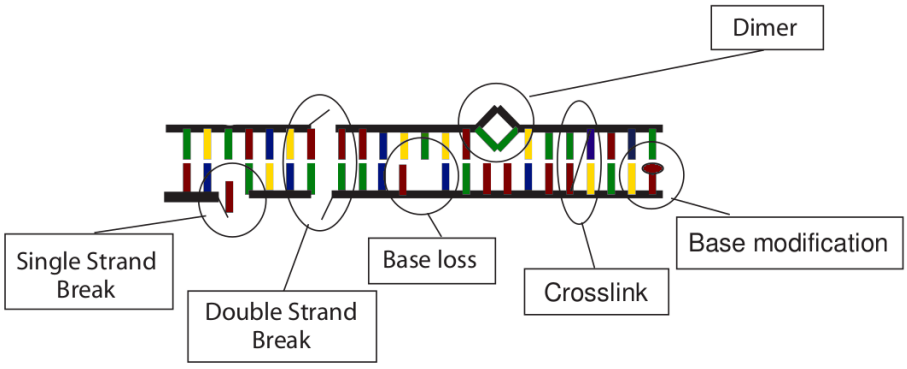

Figure 1.12: Types of possible DNA damage in cell interactions with ionizing radiation [16]

1.2.3 Relative Biological Effectiveness

The quantity that describes the effect of radiation on biological tissue is the Relative Biological Effectiveness (RBE) defined as the ratio of the radiation dose of interest to the dose of a standard radiation with the same biological effect:

$$RBE = \frac{D_{rad}}{D_{ref}} \tag{1.11}$$

The definition requires that doses have the same biological effects, but the consequences of radiation on cells are multiple and depend on cell type, radiation kind and energy. Therefore measuring the RBE value is a complex task and the uncertainties on the estimated values are significant. Experimentally, the RBE can be estimated by irradiating a sample

of cells and measuring the fraction of cells that survive. The experimental data on the number of surviving cells as a function of the dose is well described by the linear quadratic (LQ) model [10] (see Figure 1.13). The LQ model assumes that there are two components that contribute to cell death, respectively proportional to the dose and to the square of the dose:

$$S = e^{-\alpha D - \beta D^2} \tag{1.12}$$

Although the linear quadratic model is quite accurate in the dose range of conventional radiotherapy, a universal theory of cell death due to radiation exposure is not yet available. Figure 1.14 shows the RBE dependency on the linear energy transfer. The maximum value of RBE is obtained when the average distance between ionization events coincides with the diameter of the DNA double helix (2 nm). This distance corresponds to a linear energy transfer of about 100 keV/μm. For lower LET values, the distance between two ionization events is greater than the DNA diameter and the probability that a double-strand break occurs is low. At the other extreme, if the ionizing events are too close together, the dose release is higher than that required to generate a double-strand break and achieve the same biological damage.

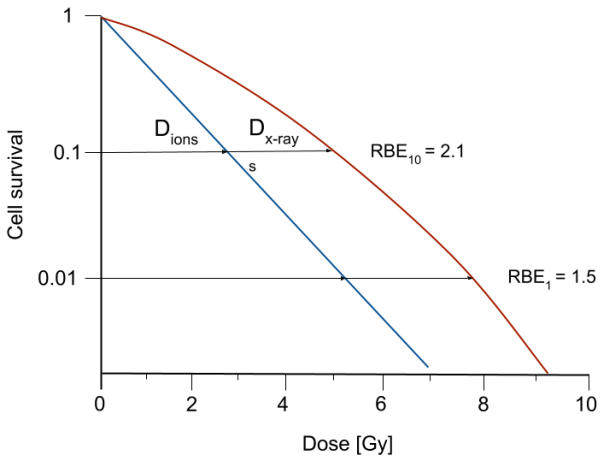

Figure 1.13: Cell survival as a function of photon (red) and ions (blue) dose [10].

Assuming the X-rays of conventional radiotherapy as reference radiation, an RBE value of 1.1 is assumed in proton therapy, considering the biological effects of protons not very different from those of photons. The carbon ion RBE varies over a wide range and a series of in vivo studies have measured a value between 1 and 3 [17]. The greater effect of protons and especially of heavy ions compared to X-rays is due to the direct damage to DNA and the higher ionization density (see Figure 1.11).

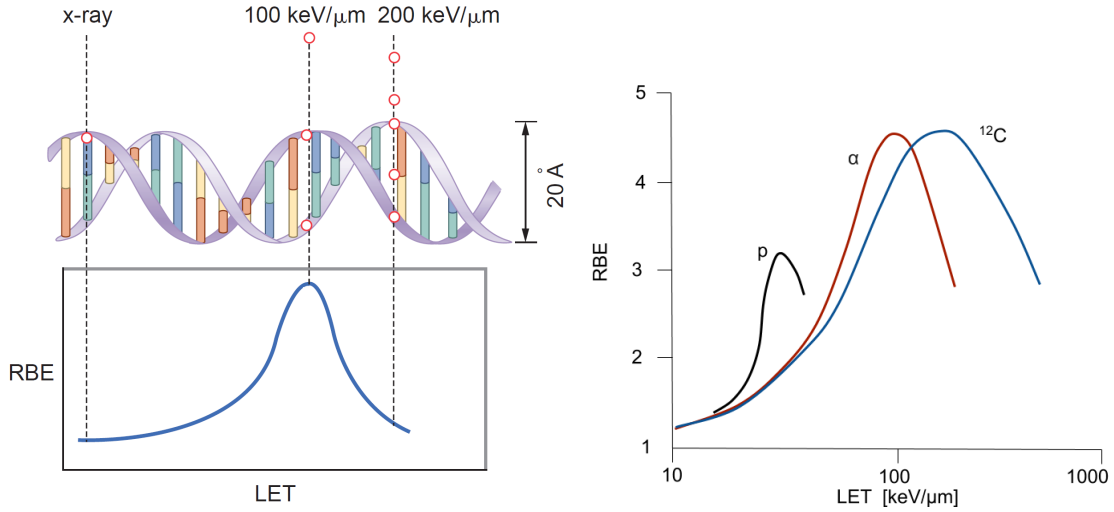

Figure 1.14: RBE as a function of linear energy transfer [15] (left). For 100 keV/μm transfer, the average separation between ionizing events coincides with the diameter of the DNA double helix. Experimental RBE as a function of linear energy transfer for protons, α particle and carbon ions [18] (right).

1.2.4 RBE and biological processes

The biological processes of tissue cells are decisive in the effect of radiation therapy. Three factors must be considered. Cells can repair damaged DNA and this capacity is greater in healthy cells than in cancerous ones. The single strand break can be easily repaired by the cell by using the opposite strand as a template, while more severe damage cannot be repaired. The repairing process occurs in a time scale of few hours. The effect of radiation is highly dependent on the oxygenation of the cell: hypoxic cells suffer less damage than aerobic ones. In diseased tissue, the hypoxic regions are frequent, especially in the core of large tumours. The effect of oxygenation on cell is the radio-sensibility and it is quantified by the Oxygen Enhancement Ratio (OER). OER is defined as the ratio between the doses to tissues with reduced and normal oxygen supply respectively, resulting in the same biological effect. The OER is generally between 2 and 3 for low LET radiation, and decreases for heavy ions. Finally, cells have different radiation sensitivity in different phases of the biological cycle. The highest radiation sensitivity is in Synthesis and in Gap 2 phases of the cell cycle [15].

1.3 Facilities and treatment

In order to ensure the safety and effectiveness of the treatment, the particle therapy requires complex technologies and an accurate treatment plan. This section summarizes the main characteristic of PT facilities and modalities of treatment.

1.3.1 Facilities

In particle therapy the beam acceleration is performed with a Linear Accelerator (LINAC), followed by a cyclotron or a synchrotron (see Figure 1.15). Cyclotrons accelerate the charged particles by means of an alternating electric field while following an outward spiral path in a static magnetic field. The beam is delivered with fixed energy, in short nano-bunches of 10^2 protons at about 100 MHz frequency. Energy variations are made by means of passive degraders and energy spread selection inside a spectrometer located at the exit of the cyclotron [19]. The synchrotron is a circular particle accelerator, in which the magnetic field, necessary to curve the trajectory of the particles, and the variable electric field, necessary to accelerate the particles, are synchronized with the beam. The variation of electric and magnetic fields allows the production of charged particle beams with different extraction energies. The carbon ion beams have a cluster structure of a few particles with a period of 100-200 ns. The period of proton beams is 3-5 times smaller and the clusters consist of 10^2 particles [19].

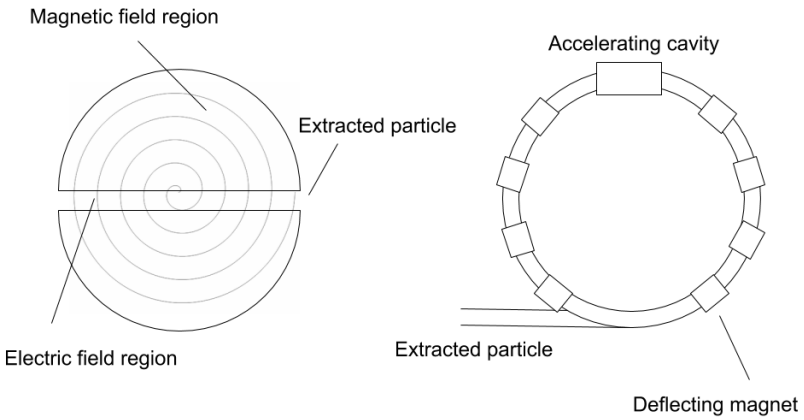

Figure 1.15: Cyclotron (left) and synchrotron (right) scheme.

The beam may be shaped by passive or active systems. In the first approach the beam is transversely widened and a shaped compensator modulates the energy, hence the range, in the different regions of the beam section. In the active systems a narrow beam is deflected by a magnetic field to deliver dose separately to each tumor voxel. In Figure 1.16 a sketch of passive and active systems is presented.

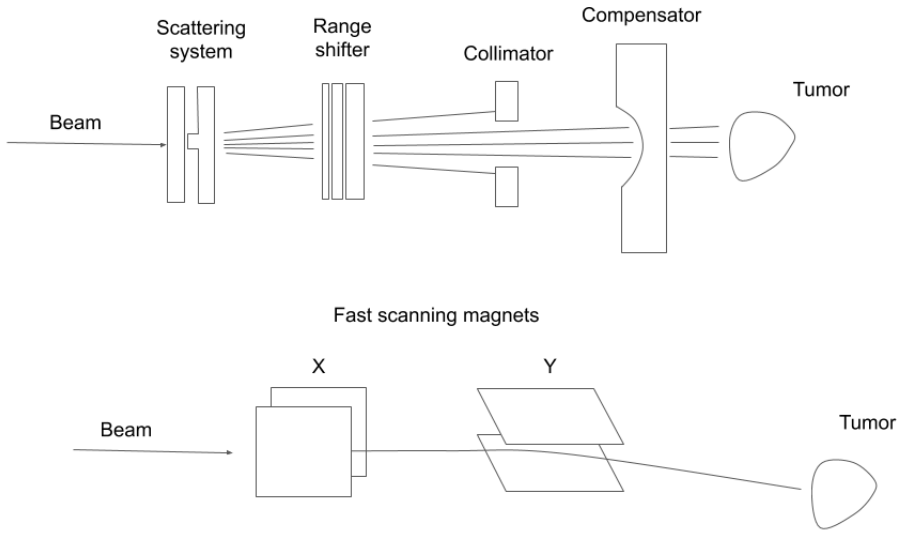

Figure 1.16: Passive (top) and active (bottom) system to shape the particle beam for the tumor treatment [12]

1.3.2 Treatment planning

The PT treatment is planned on the basis of a Computed Tomography scan (CT scan), that allows to evaluate the position and size of the tumor and study the presence of organs at risk [20]. The CT scan returns a 3D map of integer values, called "Hounsfield Unit", reflecting the X-ray attenuation coefficient. After the image acquisition, the radiotherapist defines the tumour and the volume to be irradiated, delimiting the organs at risk and other structures to be taken into account. The dose, time and beam parameters are calculated by the Treatment Planning System (TPS) by means of an analytic algorithm. In TPS the Hounsfield Unit values of CT scan are converted in stopping power map, in order to correctly estimate the required beam energy. Finally, after the treatment plan has been assessed and reviewed, the beam parameters are transferred to a database to be applied. The dose is delivered in several fractions, spread over several days. The time between fractions allows healthy cells to repair DNA damage and leads to re-oxygenation of tumor cells, increasing the probability of tumor control and reducing the side effects due to the healthy tissue exposure.

Chapter 2

Range Monitoring

The advantage of particle therapy compared to conventional radiotherapy is the spatial selectivity of dose release. This property requires high accuracy in predicting the particle range in biological tissue. However several factors can introduce significant uncertainties on the range of protons or light ions. A wrong range estimation can lead to a shift of the Bragg peak position, with a possible under-dosage of the tumour volume, and at the same time an over-dosage of healthy tissue surrounding the tumour. An error in the treatment planning can have more sever consequences in proton therapy than in photon therapy. Several sources of range uncertainty are taken into account in the treatment plane, as uncertainty in CT imaging and calibration or patient set-up. To ensure complete dose coverage of the tumor, a larger volume is irradiated providing safety margins. Safety margins are chosen by each institute and may change depending on the location of the tumour and the presence of organs at risk. At the Massachusetts General Hospital (MGH), treatment planning assumes an uncertainty in the proton beam range of 3.5% of the range plus an additional 1 mm while the University of Florida Proton Therapy Institute uses 2.5% + 1.5 mm. The range margin at MGH, for instance, results in a deliberate overshoot of 8 mm for a 20 cm range in soft tissue [21]. To reduce safety margins a feedback on particle range and dose release is increasingly necessary for more efficient and safe therapy, especially in the treatment of tumors close to organs at risk and in patients with long expectation of life, as paediatric ones. A great effort has been made in the last decades to develop on-line range and dose monitoring systems for PT applications. Unlike conventional radiotherapy, the primary beam is absorbed by the patient and cannot give information about dose release. However, different types of radiation (beta and gamma rays, neutrons, charged particles) are emitted in the nuclear interactions between the beam and the target nuclei and are related to the particle range. The development of a device for secondary radiation detection and range monitoring must meet certain requirements: achieve accuracy of about few mm, not interfere with the primary beam and patient positioning, last less than the treatment, not require changes to the treatment plan and

the dose delivery method chosen for the patient and be implemented in a treatment room, observing clinical safety regulations [22]. The future goal is to achieve a dose release control that allows for online correction of the individual beam of the treatment. Currently only some prototypes of dose monitoring at the end of the fraction have been developed and tested in clinical treatments. In this chapter, the first section describes in detail the sources of uncertainty in range estimation. The following section presents a brief overview of the devices proposed for range monitoring according to the type of radiation detected.

2.1 Range uncertainties

Uncertainties in the exact position of the distal dose may result from systematic factors, which affect all or a large part of treatment fractions, as:

- anatomical changes of patient, due, for example, to a reduction of tumor volume or to other pathologies
- CT scan calibration and resolution
- presence of artifacts in the image of the CT scan
- conversion of Hounsfield Unit in stopping-power map.

Other uncertainties are stochastic and vary from fraction to fraction, including:

- uncertainties in beam energy (compensator design and beam reproducibility)
- patient positioning
- target movements, due, for example, to breathing.

In Table 2.1 the contribute of the main factors to range uncertainty is shown. Several methods have been studied to reduce the range uncertainties, including the use of a well-known CT scan, laser control of the patient's position, beam synchronization with target movement, etc. However, the required accuracy has not yet been achieved.

Source of range uncertainty in the patient	Range Uncertainty
CT imaging and calibration	± 0.5%
CT grid size	± 0.3%
CT conversion to tissue	± 0.5%
Compensator design	± 0.2 mm
Beam reproducibility	± 0.2 mm
Patient set-up	± 0.7 mm

Table 2.1: Range uncertainties in particle therapy [21].

2.2 Range monitoring techniques

The range monitoring techniques proposed so far are mainly based on the detection of secondary radiation emitted by the interactions between beam particles and biological tissue nuclei. The emitted radiation includes neutrons, photons, charged particles, beta decay annihilation photons. Other range monitoring techniques exploit the ionoacustic waves generated by the impact of the primary beam on tissues. This section summarizes the main techniques based on secondary radiation detection.

2.2.1 PET-gamma

One of the first techniques studied for the range monitoring is based on PET (Positron Emission Tomography) photons imaging. In diagnostic PET, β^+ radioactive nuclei are administered to the patient. The positron emitted in the beta decay annihilates near the emission point with an electron of the medium, producing two gamma rays of 511 keV in opposite directions, which can be detected to reconstruct the annihilation position. In the application of PET imaging to range monitoring, the first idea was to deliver to the patient a low dose by a beam of beta radioactive nucleus (e.g. ^{19}N), followed by a beam of stable isotopes of the same element (e.g. ^{20}N). Early studies have shown that a significant amount of beta radioactive nuclei is produced by fragmentation of beam particle and target nuclei and the idea of a radioactive beam has been dismissed [23] [24].

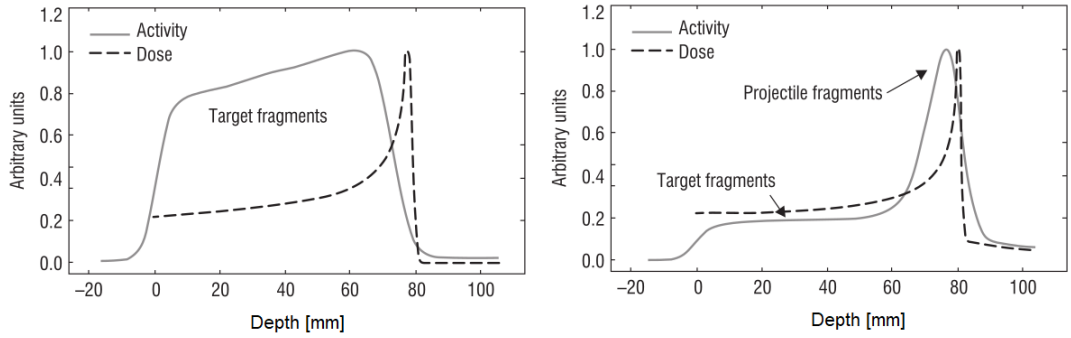

Figure 2.1: Spatial distribution of β^+ activity measured with PET imaging, for proton beam (left) and carbon ion beam (right) on PMMA [25].

Radioactive nuclei, produced by the fragmentation of the target, remain almost at rest in the place of interaction. Consequently, the spatial distribution of beta decays depends only on local nuclear interactions and grows slightly along the beam until it collapses before the Bragg peak (see Figure 2.1, left). Nuclei generated by the projectile fragmentation travel in the same direction of the beam and accumulate at their end of range, resulting in a peaked spatial distribution of the beta activity (see Figure 2.1, right). In proton therapy only the first contribution is present while in carbon ion therapy both contributions are

visible but the second is the dominant one [24]. In both cases, the most abundant positron emitters are ^{11}C, ^{15}O and ^{10}C with half-lives of 20 min, 2 min and 19 s, respectively. PET photons imaging for range monitoring in particle therapy can be applied in three different modes: in-beam, in-room and off-line. In the first mode, detection of the annihilation gammas is performed during treatment by two or more pixelated detectors. An advanced version of this technique, based on Silicon-photodetector, has been recently developed and tested in clinical environment at the Centro Nazionale di Adroterapia Oncologica (CNAO) in Pavia (Italy) [26]. In-beam monitoring has two intrinsic limits: the low statistics, two orders of magnitude lower with respect to diagnostic PET, and the background of neutrons and gamma rays, emitted by the irradiated tissues, which generate false coincidences and increase the dead time of the detectors. For this reason, PET is considered as a posteriori beam range verification rather than an online range monitoring technique. In the in-room imaging PET the gamma detection is performed at the end of the treatment fraction, thus reducing background radiation. A long data acquisition campaign was carried out from 1997 to 2008 at the Gesellschaft für Schwerionenforschung Institute (GSI) in Darmstadt, Germany. The dose of each treatment fraction of 400 patients was monitored with excellent results, thanks to two large area BGO scintillators, developed for a commercial diagnostic PET scanner. The treatment was carried out by pulsed beam and gamma ray detection took place in the time intervals between the different beam pulses and for 40 s after the end of the fraction [27]. In the off-line approach the beta emitters activity is measured after the treatment in a nearby dedicated room. The advantage of this technique is the possibility to use commercial full-ring PET scanner to monitor the patient, with fewer technological challenge compared to the development and installation of in-beam devices. Although commercial scanners cover a larger solid angle, the number of detected gamma is reduced by the low activity, due to the radioactive nuclei decay in the time interval required to move the patient from the PT room to the monitoring room. Furthermore, the biological wash-out leads to a lower spatial correlation between beta activity and dose release [24] [25].

2.2.2 Prompt gamma

In the interaction between the particle beam and the target nuclei, a large number of gamma rays are quickly emitted and therefore are an excellent feedback on the dose release. This kind of radiation is called Prompt Gamma (PG) and is emitted within 1 ns from the beam interaction. Several experimental and simulation studies have been carried out to measure yield, energy spectrum and spatial distribution of prompt gamma photons, depending on particles and beam energies. The total yield, integrated along the whole beam path, clearly depends on the beam range, i.e. beam energy, but the yield per millimeter is not heavily dependent [19]. In [28] Pinto *et al.* evaluated prompt

gamma yield per incident ion, millimeter and steradian with the following results: $(16 \pm 0.07_{stat} \pm 1_{sys}) \cdot 10^{-6}$ for 160 MeV protons, $(124 \pm 0.7_{stat} \pm 30_{sys}) \cdot 10^{-6}$ for 95 MeV/u carbon ions, $(79 \pm 2_{stat} \pm 23_{sys}) \cdot 10^{-6}$ for 310 MeV/u carbon ions. Figure 2.2 shows the experimental energy spectrum of photons emitted by the interaction of 160 MeV proton beam impinging on a water target. The prompt gamma energy spectrum is characterized by well-defined lines: the 4.44 MeV and 6.13 MeV lines are due respectively to ^{12}C and ^{16}O de-excitation, while the line at 2.2 MeV results from the de-excitation of deuterium after neutron capture by hydrogen and is not correlated to the primary beam range. The research and development of increasingly accurate simulations allowed to reach a good agreement with the experimental data, as shown in Figure 2.2.

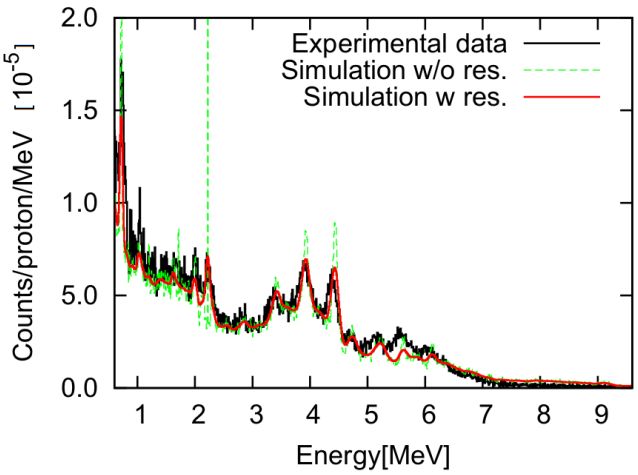

Figure 2.2: Experimental energy spectrum (black line) of photons emitted by the interaction of 160 MeV proton beam impinging on a water target, compared with the results obtained by the simulation with and without intrinsic detector resolution (red and green line) [29].

In [30] Verbung *et al.* measured the correlation between the dose released and the prompt gamma emission for the different components of the energy spectrum. The results, shown in Figure 2.3, were obtained with a proton pencil-beam, with 9 cm range, impinging on water. The total gamma emission has a slightly increasing distribution up to the Bragg peak where the primary beam particles do not have enough energy to exceed the energy threshold of nuclear reactions. The spatial distribution of prompt gamma rays therefore undergoes a rapid fall at the end of the beam. Photons at 4.4 MeV have the greatest spatial correlation with the deposited dose and therefore are the most suitable component for monitoring the primary beam range.

The main advantages of range monitoring techniques based on gamma rays are the prompt emission and the low number of interactions that change the photon direction between the emission and the detection point. The main limitation of these techniques are the

neutron background and the inability to detect the gamma ray without the photon being absorbed (photoelectric effect) or changing direction (Compton scattering). This feature requires the use of collimators to determine the photon direction (imaging systems) or the measurement of different properties of the emitted prompt gamma (non-imaging systems).

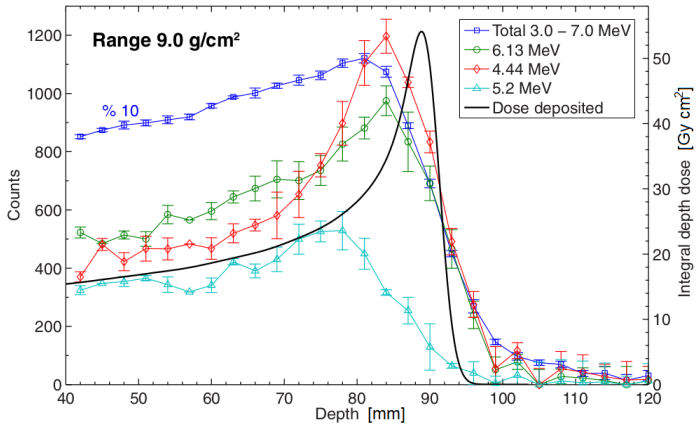

Figure 2.3: Spatial distribution of prompt gamma emission for the different components of the energy spectrum [30], obtained by a proton pencil-beam, with 9 cm range, impinging on water.

Imaging systems

Many research groups have focused their efforts on a range monitoring device based on the measurement of the prompt gamma direction through a mechanical or electronic collimator. In the first case the main challenge is to design an efficient system, able to collimate photons with a wide energy spectrum and to collect a sufficient number of events, strongly reduced by the presence of the collimator. Mechanical collimation imaging systems with a pin-hole, linear slit or multiple slits have been studied and tested [19]. The pin-hole and linear slit camera are inspired by classical optics and allow a 2D and 1D reconstruction respectively. A collaboration between the Politecnico di Milano and Ion Beam Applications SA (IBA) has developed and tested on patients a knife-edge slit camera consisting of a Tungsten collimator and a Lutetium-Yttrium OxyorthoSilicate (LYSO) detector (see Figure 2.4). The main limitation is the dependence of the resolution on the alignment of the camera with respect to the beam range [31]. A multi-slit device measures the direction of the photons through an array of collimators that allows the passage of gamma rays perpendicular to the detector. In [32] Park *et al.* developed a multi-slit camera consisting of a Tungsten collimator and two rows of 36 Caesium Iodide (CsI) scintillators. This devices is less efficient compared to slit cameras but has fewer geometric constraints and can be easily expanded [32].

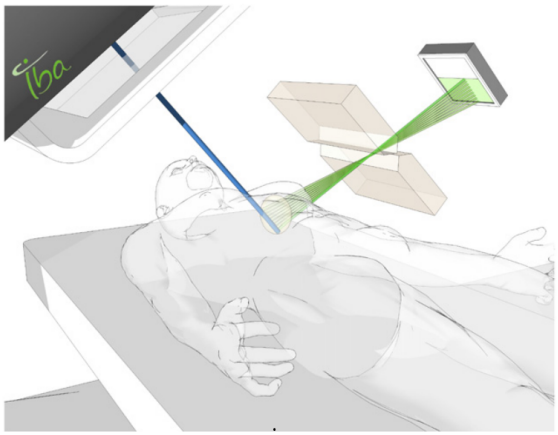

Figure 2.4: Linear slit camera developed by the collaboration between the Politecnico di Milano and IBA [31].

Active or electronic collimation is an imaging technique that measures the PG direction exploiting the Compton scattering, i.e. the elastic collision between a photon and an electron of the medium. In the Compton effect the incident photon is deflected by an angle θ according to the following relation:

$$\cos(\theta) = 1 - m_e c^2 \left(\frac{1}{E_F} - \frac{1}{E_0} \right) \qquad E_0 = E_F + E_e \tag{2.1}$$

E_e is electron energy, E_0 and E_F are the photon energies respectively before and after the scattering. Figure 2.5 shows the Compton cameras working principle. The Compton cameras reveal in a first layer the Compton interaction and in a second detector the scattered gamma ray. The measure of E_F allows to narrow the direction of emission of the primary gamma ray on the surface of a cone with opening angle θ, axis defined by the direction of the scattered gamma and vertex in the point of Compton scattering. The correct direction of the gamma ray can only be deduced from the measurement of the energy of the electron involved in the scattering.

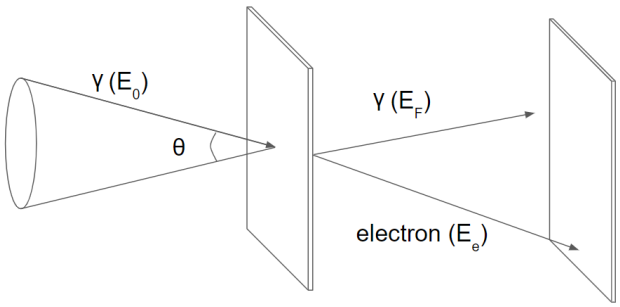

Figure 2.5: Prompt gamma imaging with Compton scattering.

For instance, in [33] a Compton camera has been developed with a stack of 6 double-sided Silicon strip detectors as scatterer and electron tracker and a Lanthanum Bromide ($LaBr_3$) scintillation crystal acting as absorber.

Non-imaging systems

The search for new methods for range monitoring led to the study of non-imaging systems based on different properties of gamma radiation (see Figure 2.6). In a facility with a pulsed beam, the Time Of Flight (TOF) measurement, as difference between the beam pulse and photon detection, allows to deduce the emission point of the prompt gamma ray. Simulations demonstrated the feasibility of the principle, showing a correlation between the beam energy, i.e. the range, and the measured time of flight (see Figure 2.6, left). The first tests of Prompt Gamma Timing (PGT) in clinical environment have given promising results [34]. The main advantage is the possibility to discriminate neutrons; however the need for a pulsed beam is a limitation of this technique. In Prompt Gamma Spectroscopy (PGS) systems the ratio between the spectral lines integrals (see Figure 2.6, right) is exploited in order to estimate the ratio between the cross sections of the different reaction channels, thus deduce the beam energy and the crossed tissue composition. In such devices an appropriate collimator system allows to analyse separately different slices of the beam [35], however reducing the available statistic. Finally, the Prompt Gamma Peak Integration (PGPI) approach measures the count rate of a series of detectors placed around the patient. The number of events observed by each detector depends on the distance from the emission points of the prompt gamma rays and an accurate analysis of the difference in count rate allows to deduce information about the ejection profile [36]. As shown in Table 2.2, energy and time of flight measure can be used individually or in combination with an imaging technique.

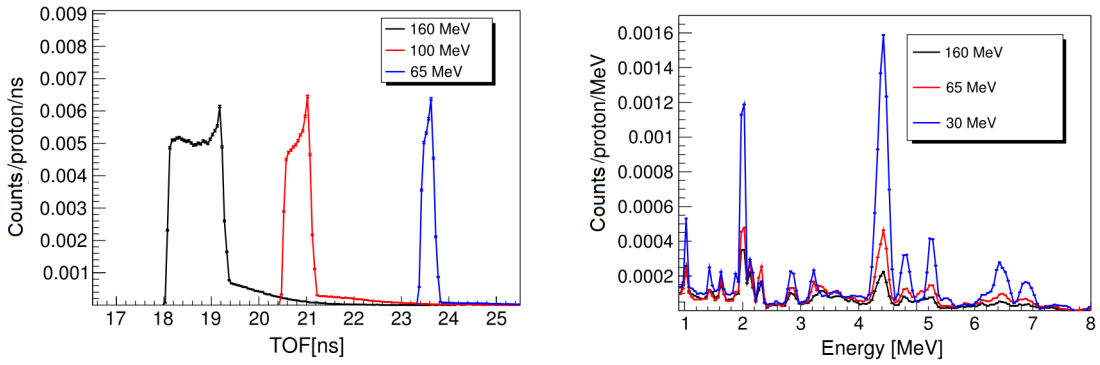

Figure 2.6: Time of flight (left) and spectra energy (right) of PG with energies larger than 1 MeV obtained from simulations of 30, 65 and 160 MeV proton beams, impinging on 1 mm thick PMMA target [19]

PG features	Imaging system		Non-imaging system		
	Mechanical collimation	Electronic collimation	PGT	PGPI	PGS
Position	✓	✓			
Energy	(✓)	(✓)	(✓)	(✓)	✓
TOF	(✓)	(✓)	✓	✓	(✓)

Table 2.2: PG modalities classified according to the PG features they exploit. Check marks in brackets mean that time of flight or energy measurements are not mandatory [19].

2.2.3 Charged particles

The fragmentation of the ion beam in the case of $Z > 1$ projectiles produces secondary charged particles, mainly proton and hydrogen isotopes, which can pass through the patient and be detected by an external device in order to monitor the beam range. Compared to gamma radiation, charged particles have very different properties, hence different advantages and limitations if considered as a range monitoring technique. The charged particles can be detected with almost 100% efficiency and can be tracked with two or more active planes without collimators. However, the statistic is low, due to absorption into the tissues depending on their production energy, and the reconstruction spatial resolution is affected by multiple scattering within the patient. Several studies have been carried out to measure the number of charged particles produced by a therapeutic ^{12}C beam impinging on a tissue equivalent target, correlating the spatial distribution with the dose released (see Figure 2.7).

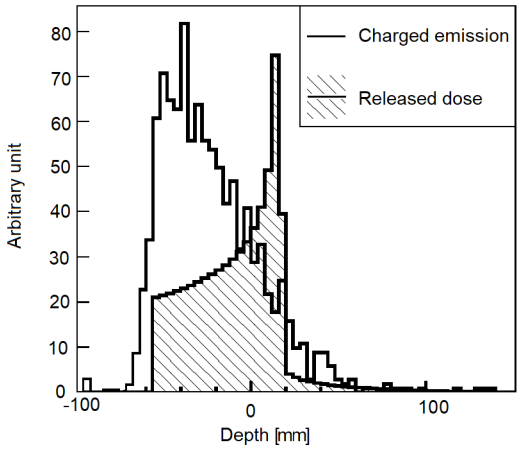

Figure 2.7: Simulated depth-dose distribution (dashed area) superimposed on the measured longitudinal profile of charged secondary particles, with a 220 Mev/u carbon ion beam on PMMA [37].

Most projectile fragments are produced in the direction of the primary beam, however, on the basis of simple geometrical considerations, the detection of charged particle at large angles corresponds to a better spatial resolution in range monitoring [38]. Therefore the choice of the angle between the primary beam and the detector is always a trade-off between efficiency and resolution [39][38]. The Innovative Solutions for Dosimetry in Hadrontherapy (INSIDE) collaboration proposed an innovative bi-modal imaging concept that combines an in-beam PET scanner with a tracking system for charged particle imaging. The particle tracking is performed by the Dose Profiler, a multi-layer scintillating fiber tracker [40].

2.3 Research and development

Comparing the different approaches of range monitoring, it is necessary to take into account resolution, efficiency, measurement duration, possibility to be integrated in a clinical environment, applicability to different beams (pulsed, continuous) and to different primary beam particles (protons, carbon ions, etc.). Nowadays, the proposed techniques do not meet all the requirements. Research and development in range monitoring techniques have to include:

- new experimental measurement campaigns of secondary radiation in different types of treatment
- development of increasingly accurate simulations for an increased ability to correlate the detected radiation and dose profile
- development of new techniques of radiation detection
- combinations of several techniques in order to achieve the required performance.

The PAPRICA project, object of this thesis, is part of this branch of research and proposes an innovative method for range monitoring, based on prompt gamma imaging.

Chapter 3

The PAPRICA chamber

The main goal of the PAPRICA (PAir PRoduction Imaging ChAmber) project is to demonstrate the feasibility of an online beam range monitoring in proton therapy, exploiting the Pair Production (PP) mechanism to detect and backtrack prompt gamma radiation. This technique was developed in astrophysics applications for high energy cosmic photon imaging [41] [42], but has never been explored in the prompt gamma energy range, due to the low pair production cross section. The prompt gamma imaging by means of the pair production mechanism is hence a new technique in particle therapy range monitoring and exploits mainly prompt gamma rays with energies equal or larger than 4 MeV, the spectrum component most related to the Bragg peak (see Section 2.2). In pair production a photon with energy greater than 1.022 MeV interacts with matter, converting its energy into a electron-positron pair. This effect can only occur in the presence of a third charged body, usually a nucleus, which receives a fraction of the photon energy, in order to conserve the system total momentum.
The goal of PAPRICA is to detect the electron and the positron, generated in the pair production of a prompt gamma ray, and reconstruct the photon direction by means of the measurement of the pair four-momentum. The momentum acquired by the nucleus is a not-accessible parameter and consequently must be neglected, introducing an intrinsic limit in photon reconstruction, hence in the achievable spatial resolution on the single prompt gamma ray reconstruction. The photon backtracking is implemented in three steps: conversion of the PG into a positron and an electron (pair production mechanism), measurement of positron and electron four-momentum, calculation of the PG direction. The pair production occurs in a layer, called converter, whose main purpose is to maximize the number of pair generated. The electron and positron direction is measured by a tracker, consisting of multi-plane pixelated detector. In each plane the two leptons release a signal, forming a track which allows to determine the direction of their momentum; the magnitude is measured by a calorimeter placed after the tracker. A sketch of the PAPRICA detector is shown in Figure 3.1. The PAPRICA detector has different objectives

and constraints compared to cosmic rays detectors and, in particular, the chamber technology choice was driven by some key aspects: photon backtracking resolution compatible with the requirements set by particle therapy monitoring applications, maximisation of the collectable statistics, integration in a clinical environment.
PAPRICA has several advantages over other gamma-based imaging techniques. First of all, the proposed method mainly exploits gamma rays at energies higher than 4 MeV, reducing the background from lower-energy photons induced by neutrons unrelated to the Bragg peak. In addition, the PAPRICA chamber does not require collimators or time of flight information and can therefore be easily integrated into a clinical environment. Neutrons can be discriminated studying the topology of a pair production event in the chamber, allowing for a range monitoring both in proton and carbon ion therapy.
The aim of this chapter is to describe the PAPRICA chamber, both from the point of view of the physics involved and the technology adopted. In particular, the mechanism of pair production, the choice of detectors and the backtracking algorithm will be presented.

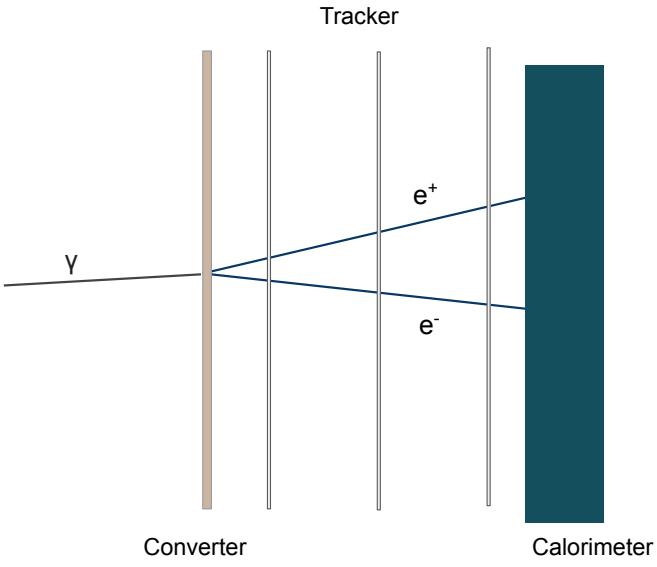

Figure 3.1: Sketch of the PAPRICA chamber consisting of a converter, a tracker and a calorimeter.

3.1 PAPRICA physics

The dynamic of prompt gamma ray detection in the PAPRICA chamber involves different types of interactions. This section presents an in-depth examination of the mechanism of pair production and a brief review of the electron and positron interaction with matter.

3.1.1 Photon interactions

The interaction between gamma rays and matter is governed by three phenomena: photoelectric effect, Compton scattering and pair production. The photoelectric effect involves the absorption of a photon by an atomic electron with the subsequent ejection of the electron from the atom. Compton scattering is the collision of photons on free electrons. Although in matter the electrons are bound, if the photon energy is high with respect to the binding energy, the electrons can be considered as essentially free. Finally, as briefly described above, the pair production involves the formation of a pair of leptons in the field of a nucleus. The cross section of gamma interactions depends on the photon energy and the atomic number of the material involved (see Figure 3.2). At low energy (< 0.5 MeV) and high atomic number the dominant interaction is the photoelectric effect. The relative importance of the Compton scattering increases with energy, particularly for low atomic number materials. Pair production has an energy threshold of 1 MeV and is the dominant effect for high energy (> 5 MeV) and high atomic number.

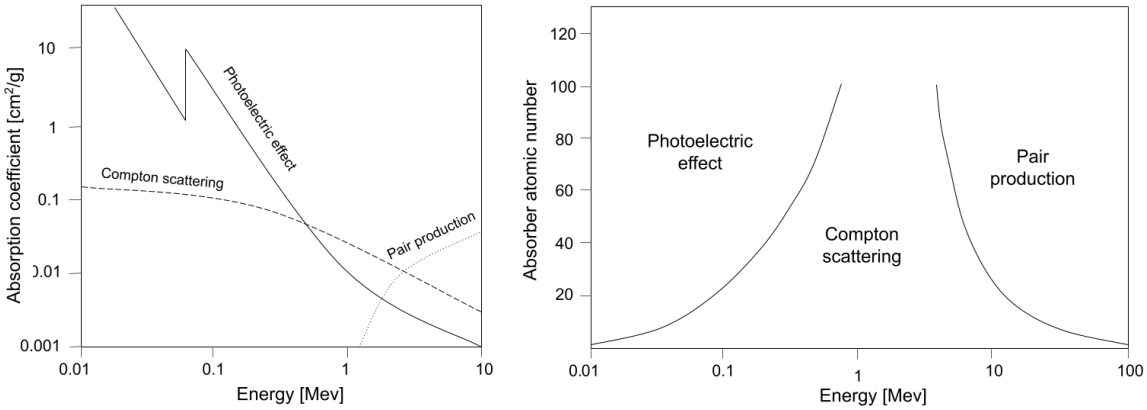

Figure 3.2: Absorption cross section of the three main types of gamma ray interaction in Lead (left) and relative importance as a function of the photon energy and atomic number of the absorber (right), adapted from [43].

3.1.2 Pair production

The pair production mechanism was discovered in 1933 by Patrick Blackett and Giovanni Occhialini, by taking photographs of electrons and positrons created from cosmic rays in a Wilson cloud chamber [44]. A sketch of a pair production event is shown in Figure 3.3.

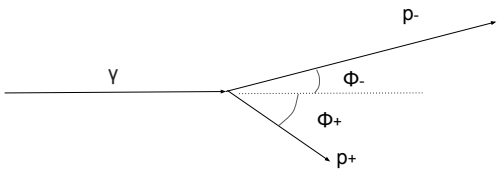

Figure 3.3: Pair production: $\mathbf{p}_\gamma$, $\mathbf{p}_+$ and $\mathbf{p}_-$ are respectively the gamma, positron and electron momentum while ϕ_+ and ϕ_- are the angles between the gamma direction and the leptons directions.

In PP momentum and energy conservation laws require (the c constant is implied):

$$p_\gamma = p_+ \cos\phi_+ + p_- \cos\phi_- \tag{3.1}$$

$$p_+ \sin\phi_+ = p_- \sin\phi_- \tag{3.2}$$

$$p_\gamma = \sqrt{(p_+)^2 + m_0^2} + \sqrt{(p_-)^2 + m_0^2}; \tag{3.3}$$

Equation 3.3 set a cut-off equal to $2m_0$ =1.022 MeV in the photon energy for the generation of an electron-positron pair. From Equation 3.1 and Equation 3.3 follows:

$$p_+ \cos\phi_+ + p_- \cos\phi_- = \sqrt{(p_+)^2 + m_0^2} + \sqrt{(p_-)^2 + m_0^2} \tag{3.4}$$

The left side of the equation is larger than the right side for any real momentum value. This simple model shows that the conservation of energy and momentum cannot be achieved simultaneously without the introduction of a third body acquiring a fraction of the photon energy and momentum. The body may be a nucleus or an electron of the material. However, the pair production in the field of an electron is a negligible phenomenon compared to the first one and therefore will not be treated. The nucleus is much more massive than the leptons involved and can absorb a fraction of the photon momentum without a significant increase in kinetic energy. The recoil momentum of the nucleus is equal to:

$$p_N = p_\gamma - p_+ \cos\phi_+ - p_- \cos\phi_- \tag{3.5}$$

Let consider the simple case in which the electron and the positron are emitted at the same angle with respect to the direction of the photon. The angle between the two leptons can be defined as $\phi \equiv 2\phi_+ = 2\phi_-$. In this case the electron and positron are emitted with the same momentum p and the same energy $E_\gamma/2$ (see Equation 3.2 and Equation 3.3).

The nucleus recoil is therefore:

$$p_N = p_\gamma - 2p \cos\frac{\phi}{2} \tag{3.6}$$

$$p_N = E_\gamma - 2\sqrt{\frac{E_\gamma^2}{4} - m^2} \cos\frac{\phi}{2} \tag{3.7}$$

The result obtained with this simple model shows that the nucleus recoil increases with the electron-positron angle ϕ and decrease with photon energy E_γ.
Experimental measurements have shown that the cross section of pair production is increasing with the energy of the photon and is proportional to the square of the atomic number of the nucleus involved (Z^2). Several models have been developed to calculate the pair production cross section. The main challenge is to accurately describe the interaction over a wide range of photon energies, considering the effects of finite nucleus size and electron screening. A review of the proposed models has been made in [45]. In [46] Barò *et al.* proposed a semi-empirical model from Bethe-Heitler theory, which takes in account electron screening and adds correction factor to extend the cross section to low and high energies. The relative difference between the cross section of Barò model and the cross section tabulated are appreciable near the threshold (1.022 MeV), but decrease rapidly with increasing photon energy. At E = 3 MeV, the differences reduce to 4% and do not exceed 2% for energies larger than 6 MeV for almost all the elements. Figure 3.4 shows the cross section dependence on the fraction ϵ of photon energy acquired by the electron, called reduced energy.

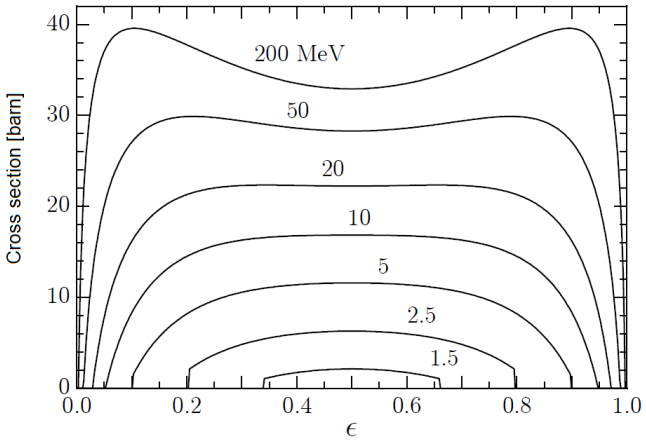

Figure 3.4: Theoretical cross section dependence on electron reduced energy. The trends for different photon energy are shown [47].

The Barò theory predicts that the pair production cross section, considered as a function of the electron reduced energy, is symmetrical around $\epsilon = 0.5$. This trend is reasonably

accurate only for photon energies larger than 5 MeV. For lower photon energies, the effect of the electrostatic field of the atom (which slows down the electron and accelerates the positron) becomes increasingly important, with the result that electron energy distribution becomes asymmetrical with a mean value less than 0.5. As the final state involves three bodies (the nucleus and the produced pair), the directions of the produced particles cannot be obtained from only their kinetic energies. The distribution of the angle between particles and photon directions may be calculated only in the high energy limit with the following result [47]:

$$P(\cos\phi_{\pm}) = a(1 - \beta_{\pm}\cos\phi_{\pm})^{-2} \tag{3.8}$$

where a is a normalization constant and

$$\beta_{\pm} = \frac{\sqrt{(E_{\pm} - m_0c^2)(E_{\pm} + m_0c^2)}}{E_{\pm}} \tag{3.9}$$

3.1.3 Electron and positron interactions

The main processes that drive the energy loss of light charged particles, such as positrons and electrons, are the multiple scattering with the electrons of the medium and the emission of bremmstrahlung radiation. Multiple scattering differs from the interaction of heavy charged particles by the comparable mass of the projectile and the target. In each interaction an electron or a positron can suffer a high energy loss and be diverted in another direction. The energy loss due to multiple scattering is equal to [7]:

$$-\frac{dE}{dx} = 2\pi N_a r_e^2 m_e c^2 \rho \frac{Z}{A}\frac{1}{\beta^2}\left[\ln\frac{m_e^2c^4\tau^2(\tau+2)}{2I} + F(\tau)\right] \tag{3.10}$$

where τ is the kinetic energy of particle in units of m_ec^2, while the others variables and constants are described in Section 1.1. In the bremmstrahlung effect the leptons lose energy in the form of electromagnetic radiation. The radioactive emission occurs when the particle is deflected by the interaction with a nucleus of the medium. The ratio between bremmstrahlung and collision energy loss is given approximately by $E \cdot Z/700$ [48]. Therefore, at the energies of interest for the PAPRICA detector, the bremsstrahlung effect is a secondary energy loss and does not play a key role in the dynamics of the chamber (see Figure 3.5). In addition to the interactions mentioned above, the positron can annihilate itself with an electron of the medium producing two 511 KeV gamma rays.

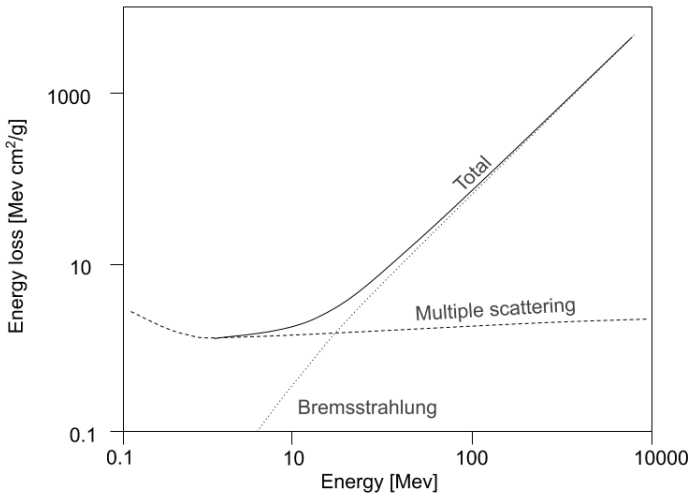

Figure 3.5: Light particle energy loss due to multiple scattering and bremmstrahlung [7].

3.2 Detectors

3.2.1 Converter

The first step for the reconstruction of the incident PG is the production of an electron-positron pair. This process takes place in the converter. After pair production, electron and positron cross the converter along the direction of the original prompt gamma ray, interacting with the surrounding medium. The main interaction mechanisms are the multiple scattering and the positron annihilation with the electrons of the converter medium. These interactions lead to a loss of information of the momentum and the energy of the particles or, in the worst case, to their absorption. The purpose of the converter is therefore to maximize the efficiency of producing pairs and at the same time minimizing the interactions between particles and matter. The pair production cross section depends on the atomic number of the medium according to the law Z^2, while multiple scattering is proportional to Z. The atomic number choice is hence a trade-off between maximum PP efficiency and the minimum particle momentum loss in terms of magnitude and direction. Four different materials have been studied, two active, i.e. able to generate a signal that can be detected when a charged particle crosses it, and two passive. An active converter allows to set a trigger that requires the time coincidence between the signals in the converter and the calorimeter, thus selecting the pair production events. In addition, in a pixelated detector the signal allows to know the position of the vertex with the precision given by the pixel size. The materials proposed and their characteristics are shown in Table 3.1. BC404 plastic is a scintillator material that generates a detectable light signal if an energy release occurs inside it. It is a low atomic number material, therefore characterized by a low conversion efficiency. Lutetium-Yttrium OxyorthoSilicate, also known as LYSO, is an inorganic scintillating crystal with chemical formula $Lu_{2(1-x)}Y_{2x}SiO_5$. It is a mate-

rial with excellent scintillation properties and often used in the construction of diagnostic PET detectors. However, 2.6% of naturally Lu is ^{176}Lu, a long-lived radioactive element including a beta decay, with 593 keV maximum energy, and three simultaneous gamma decays (88 keV, 202 keV, 307 keV), which generate a background in LYSO scintillator. This background may be removed by setting a threshold in energy on the radiation to be detected or by the request of a time coincidence with another detector. The LYSO advantage, compared to plastic, is the higher atomic number that leads to a higher efficiency in pair production. Tungsten is a cheap material with high atomic number and thanks to these property it is a good candidate for a passive converter, as well as lead.

Material	Symbol	Z	Density [g/cm^3]
Plastic	BC404	4	1.0
Lutetium-Yttrium OxyorthoSilicate	LYSO	66	7.4
Tungsten	W	74	19.3
Lead	Pb	82	11.3

Table 3.1: Proposed converter materials.

For thin layer, the number of pair generated is proportional to thickness δz, according to the approximate equation:

$$N_{pp} = \sigma_{pp} \cdot \delta z \cdot N_\gamma \tag{3.11}$$

σ_{pp} is the cross section of pair production, N_γ the number of prompt gamma rays. On the other hand multiple scattering depends on the number of collisions and therefore on the distance of electron and positron path. As a result, the choice of thickness is a trade-off between pair production efficiency and reduction of multiple scattering effects.
The choice of material and thickness of the converter will be one of the steps of detector optimization and will play a key role in the performance of the chamber. The surface of the converter will be equal to 20 x 5 cm^2 to exploit the entire surface of the chosen tracker.

3.2.2 Tracker

The purpose of the tracker is to measure the direction of the electron and positron momentum. The tracker must meet the following requirements: high tracking efficiency to maximize the number of pair detected, reduced material budget in order to minimize the multiple scattering suffered by the particles and high spatial resolution to achieve the best possible precision on the production vertex. The detector chosen for particle tracking is the ALPIDE (ALice PIxel DEtector) [49]: a MAPS (Monolithic Active Pixel Sensor) developed by the ALICE collaboration at CERN. The ALPIDE is a sensor with CMOS technology of dimensions of 15 x 30 mm^2 with an array of 512 x 1024 pixels of 27 x 29 μm^2. The interface, control and reading functions are implemented in a peripheral region 1.2 x 30 mm^2, which constitutes a dead zone of the sensor. Several tests on pion and protons

beams performed at PS (CERN) and in DESY (Hamburg) have shown that the ALPIDE has a tracking efficiency greater than 99%, with a rate of 10^{-9} fake-hits per pixel and event. The tracker will consist of 3 planes, called HIC (Hybrid Integrated Circuit). Each HIC is a matrix of 7 x 2 ALPIDEs for a surface of 21 x 3 cm^2. An experimental study of interest for the reconstruction of prompt photons through the production of pairs, with the aim of rejecting the background, is the measurement of the of the cluster size, i.e. the number of pixels belonging to a single cluster, generated by electron or positron.
ALPIDE is the state of the art technology in the field of charged particle trackers and meets the requirements of the PAPRICA chamber. The spatial resolution that can be achieved by the tracker is much higher than the intrinsic resolution on the reconstructed photon, determined by the recoil of the nucleus and the multiple scattering in the converter. On the other hand it is a detector already developed and carefully tested by ALICE collaboration, ideal for a feasibility study of a new technique. The optimization of the tracker will consist in the choice of the optimal distance between the HIC planes, taking into account the mechanical constraints of this technology.

3.2.3 Calorimeter

The purpose of the calorimeter is to measure the momentum of the leptons as well as to provide a trigger for the data acquisition. Electron and positron momentum measurement is an essential step for a correct reconstruction of the incident gamma direction as will be described in the next section. The calorimeter must be pixelated in order to separately detect the electron and positron and discriminate the background events. The main request that drives the choice of material and size of the calorimeter is a good energy resolution and low backscattering of positron and electron from the calorimeter surface. The backscattered particles release only a fraction of the energy in the calorimeter and may cross the tracker ALPIDEs, increasing the background. Therefore an organic plastic scintillator with low atomic number and low backscattering cross section was chosen. The materials property are reported in Table 3.2.

Material	Symbol	Z	Density [g/cm^3]
Plastic	EJ212	4	1.023

Table 3.2: Proposed calorimeter material [50].

The size of the calorimeter pixels is a parameter to be optimized, in order to ensure the separation of the electron and positron signals and the containment of the pair in the calorimeter.

3.3 Reconstruction algorithm

The reconstruction algorithm of the prompt gamma ray allows to estimate the position of the photon emission from the measurement of the leptons momentum. The prompt gamma reconstruction involves the calculation of three quantities: pair production vertex in the converter, photon momentum and gamma ray emission point.

3.3.1 Vertex calculation

In theory, the pair production position is the vertex where electron and positron linear trajectories meet. In the real case, the multiple scattering in the converter and inside the three HICs of the tracker changes the particle direction and the lines defined by their momentum do not have an intersection point in the three-dimensional space. A good approximation of the vertex position is the Point Of Closest Approach (POCA), found as the midpoint of the Distance Of Closest Approach (DOCA). In the parametric form the straight lines $P(t)$ and $Q(s)$ are defined by a point P_0,Q_0 and a vector $\mathbf{u}$, $\mathbf{v}$:

$$\begin{aligned} \mathbf{P}(t) &= \mathbf{P}_0 + t\mathbf{u} \\ \mathbf{Q}(s) &= \mathbf{Q}_0 + s\mathbf{v} \end{aligned} \tag{3.12}$$

Let $\mathbf{w}(t,s) = \mathbf{P}(t) - \mathbf{Q}(s)$ be a segment between the lines. The goal is to find the parameters s_m and t_m that minimize the w length.

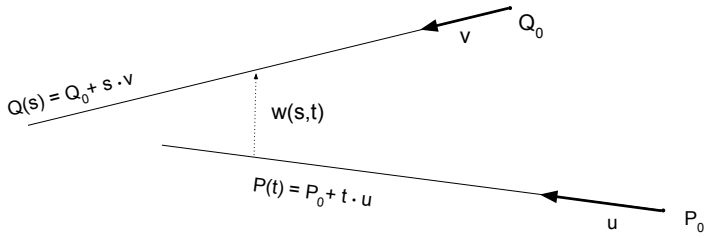

Figure 3.6: Minimum distance between lines in 3D.

If lines are not parallel and do not intersect each other, DOCA is defined by the segment simultaneously perpendicular to both lines (see Figure 3.6), and this is equivalent to satisfying the two equations:

$$\begin{aligned} \mathbf{u} \cdot \mathbf{w} &= 0 \\ \mathbf{v} \cdot \mathbf{w} &= 0 \end{aligned} \tag{3.13}$$

These two equations may be solved by substituting $\mathbf{w} = \mathbf{w}_0 + t\mathbf{u} - s\mathbf{v}$, where $\mathbf{w}_0 = \mathbf{P}_0 - \mathbf{Q}_0$, to get two simultaneous linear equations:

$$\begin{aligned} (\mathbf{u}\cdot\mathbf{u})t - (\mathbf{u}\cdot\mathbf{v})s &= -\mathbf{u}\cdot\mathbf{w_0} \\ (\mathbf{v}\cdot\mathbf{u})t - (\mathbf{v}\cdot\mathbf{v})s &= -\mathbf{v}\cdot\mathbf{w_0} \end{aligned} \tag{3.14}$$

Defining the following parameters:

$$a = \mathbf{u}\cdot\mathbf{u} \quad b = \mathbf{u}\cdot\mathbf{v} \quad c = \mathbf{v}\cdot\mathbf{v} \quad d = \mathbf{u}\cdot\mathbf{w_0} \quad e = \mathbf{v}\cdot\mathbf{w_0} \tag{3.15}$$

the minimum length of w corresponds to:

$$\begin{aligned} t_m &= \frac{be - cd}{ac - b^2} \\ s_m &= \frac{ae - bd}{ac - b^2} \end{aligned} \tag{3.16}$$

When $ac - b^2 = 0$, the two equations are dependant, the two lines are parallel, and the distance between the lines is constant. Otherwise the midpoint of segment $\mathbf{w}(t_m, s_m)$ defining the point of closest approach, i.e. the best vertex approximation, may be found as:

$$\mathbf{POCA} = \frac{\mathbf{P}(t_m) + \mathbf{Q}(s_m)}{2} \tag{3.17}$$

3.3.2 Photon momentum

The photon momentum is computed from the momentum conservation in pair production, neglecting the nucleus recoil:

$$\mathbf{p}_\gamma^{reco} = \mathbf{p}_+ + \mathbf{p}_- \tag{3.18}$$

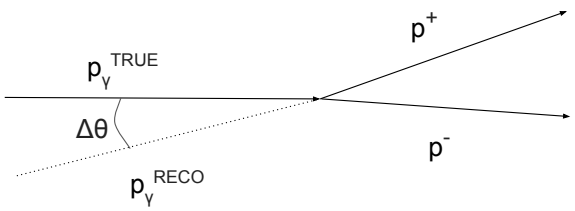

Figure 3.7: Photon momentum reconstruction.

Equation 3.18 may be re-written by separating the magnitude and the direction of particle and gamma photon momentum

$$\hat{\mathbf{p}}_{\gamma}^{reco} = \frac{p_{-}}{p_{\gamma}^{reco}}\,\hat{\mathbf{p}}_{+} + \frac{p_{+}}{p_{\gamma}^{reco}}\,\hat{\mathbf{p}}_{+} \tag{3.19}$$

In this equation the direction of the photon is given by the weighted sum of the electron and positron directions, where the weight is given by the fraction of the photon momentum acquired by each particle. The true direction of the prompt gamma ray and the reconstructed direction differ by an angle ($\Delta\theta$) mainly due to the intrinsic effects such as nucleus recoil and multiple scattering in the converter:

$$\Delta\theta = \frac{\mathbf{p}_{\gamma}^{reco} \cdot \mathbf{p}_{\gamma}^{true}}{p_{\gamma}^{reco} p_{\gamma}^{true}} \tag{3.20}$$

$\Delta\theta$ varies depending on the fraction of photon momentum acquired by the nucleus and the stochastic events of the multiple scattering. The average of the expected distribution (see Figure 3.7) is the angular resolution of the chamber and depends on the converter material and thickness.

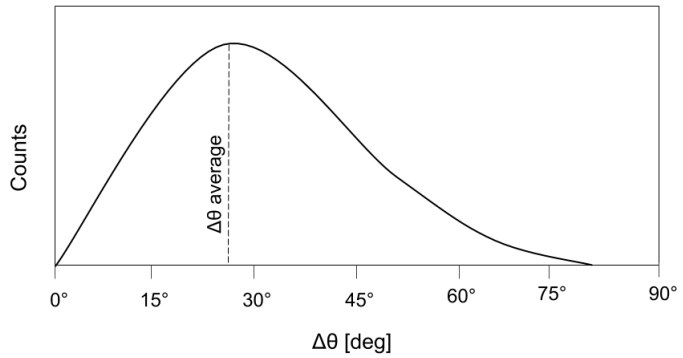

Figure 3.8: Distribution of the angle between true and reconstructed photon momentum.

3.3.3 Photon emission point

The last step needed to reconstruct the spatial distribution of the prompt gamma ray is the calculation of the position of photon emission. If the source distance from converter is known, the direction of the photon can be projected from the reconstructed vertex to a plane containing the source and parallel to the front side of the converter.

Let define the gamma direction as:

$$\mathbf{P(s)} = \mathbf{P_0} + s\mathbf{u} \tag{3.21}$$

The plane containing the source may be individuated by a normal vector $\mathbf{n}$ and a point $\mathbf{Q}$ (see Figure 3.9). If $n \cdot u = 0$, the line is parallel to the plane and never intersects it.

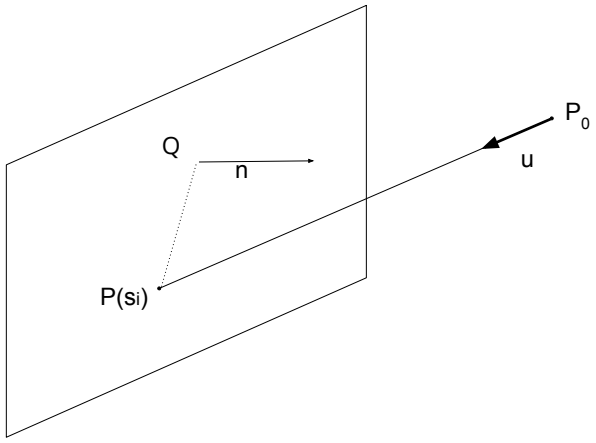

Figure 3.9: Intersection between a straight line and a 3D plane.

Otherwise the line intersects the plane in a unique point $\mathbf{P}(s_i)$, which may be individuated requesting that the normal vector of the plane and the vector $\mathbf{Q} - \mathbf{P}(s_i)$ are perpendicular

$$\mathbf{n} \cdot (\mathbf{Q} - \mathbf{P}(s_i)) = 0 \tag{3.22}$$

Equation 3.22 is equivalent to:

$$\mathbf{n} \cdot (\mathbf{Q} - \mathbf{P_0} - s_i\mathbf{u}) = 0 \tag{3.23}$$

with solution:

$$s_i = -\frac{\mathbf{n} \cdot (\mathbf{Q} - \mathbf{P_0})}{\mathbf{n} \cdot \mathbf{u}} \tag{3.24}$$

The reconstructed points on the source plane, one for each pair production event, are distributed around the source with a dispersion given by the angular resolution and the distance of the converter from the source. In fact, as can be deduced from simple geometric considerations, the distance between the source and the calculated emission point increases with the distance between the source and the chamber. The spatial distribution obtained may be analyzed, projecting it on the axes of the plane. In the case of a point source, on the two axes a Gauss distribution, given by the statistical uncertainties of each event, is expected, as shown in Figure 3.10. The standard deviation σ of the distribution returns

the spatial resolution on single event, while the mean of the Gauss distribution returns the reconstructed source position. If N is the number of events detected, the average is subject to a δ error, called standard error, equal to (Central Limit Theorem):

$$\delta = \frac{\sigma}{\sqrt{N}} \tag{3.25}$$

Hence increasing the number of detected events decreases the uncertainty on the mean value and the position of the source can be reconstructed with greater accuracy. The trade-off between the production efficiency of the pairs, therefore the number of reconstructed events, and the resolution on the single event has been subject of study of this thesis.

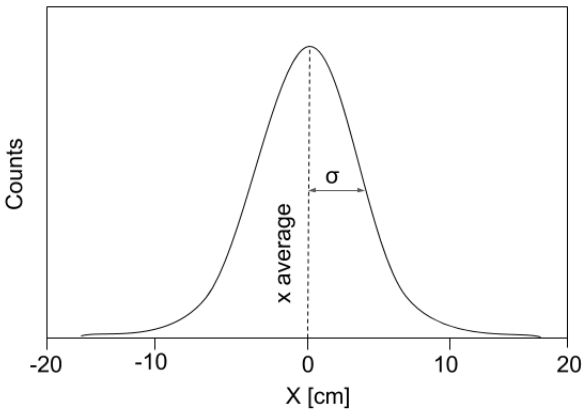

Figure 3.10: Example of the reconstruction of gamma emission point on an axis of the source plane. The dispersion around the true value is due to the finite angular resolution in reconstructing the photon direction.

Chapter 4

Events dynamic

The aim of this chapter is to introduce the fundamental quantities in the study and optimisation of PAPRICA performance. After an introduction on the FLUKA Monte Carlo code, the results obtained from the simulation of a particular detector design will be presented. Although the results are exclusively referred to the simulated geometry described in Section 4.1, the trend of the analyzed quantities will be the ground base of the chamber design optimization studied in Chapter 5.

4.1 Monte Carlo simulations

Monte Carlo (MC) codes are increasingly spreading in the hadrontherapy community due to their detailed description of radiation transport and interaction with matter. The FLUKA code has been chosen in this thesis, as it is well benchmarked for particle therapy applications.

4.1.1 The FLUKA code

FLUKA is jointly developed by the European Organization for Nuclear Research (CERN) and the Istituto Nazionale di Fisica Nucleare (INFN) [51] [52] [29]. This code is used in many applications such as, for example, proton and electron accelerator shielding, target design, calorimetry, activation, dosimetry, detector design, cosmic rays and radiotherapy. It can simulate a large number of different particles covering a wide energy range (from keV to TeV). FLUKA rests on updated physical models, based as far as possible on well tested microscopic models. The microscopic approach preserves correlations among particles physical quantities, and it provides predictions where no experimental data are available. The physical models are fully integrated in the code and cannot be modified. However, a set of user interface routines, written in Fortran, can be used to customise the software and control each step of the simulation. Very complex geometries can be handled, thanks to an improved version of the Combinatorial Geometry (CG) package. Various visualisation

and debugging tools are also available, as the graphical interface Flair, which includes the high-level management of the entire simulation process, the geometry generation and material assignment.

4.1.2 PAPRICA simulations

The simulations were performed using a photon point source, located 30 cm from the converter, along the Z-axis perpendicular to the detector surface. As already experienced in developing other monitoring devices, it is known that distances of the order of 30 cm are compatible with the monitor operation inside a treatment room [53]. The emission of photons is in a cone irradiating the converter surface to minimize the simulation CPU time. An example of PAPRICA geometry developed in Flair is shown in Figure 4.1: the converter is a LYSO layer of 1.5 mm thickness and 3 x 21 cm^2 area; the tracker, placed at 0.5 cm distance, consists of 3 planes 3 x 21 cm^2 of MAPS ALPIDEs with an interplane distance of 2 cm; the plastic (EJ212) scintillator calorimeter with a 5 x 21 cm^2 surface and 4 cm depth is located at 0.5 cm from the last tracker plane.

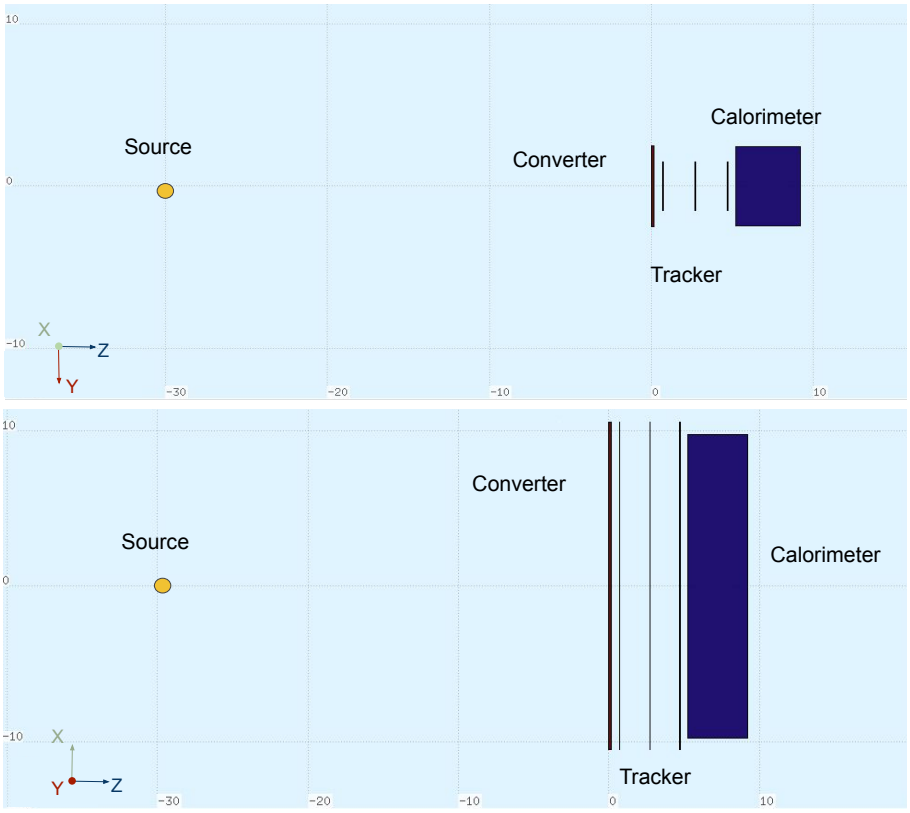

Figure 4.1: Example of PAPRICA geometry designed by Flair graphic interface. The Y-Z (top) and X-Z (bottom) views are shown. The source, indicated by the yellow circle, is located at 30 cm from the converter.

The energy spectrum of the source has been simulated as the prompt gamma spectrum obtained from a simulation of a 160 MeV proton beam on a PMMA parallelepiped, which well approximates the density and the atomic characteristics of biological tissues (see Figure 4.2).

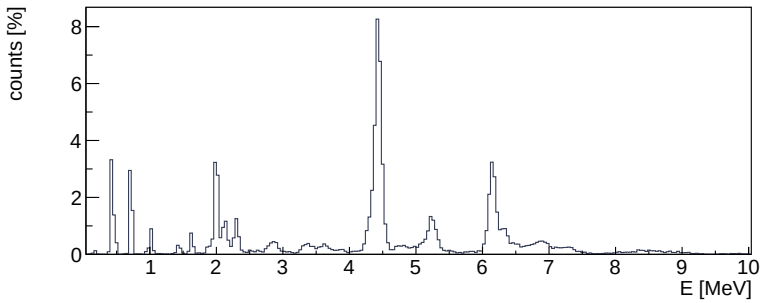

Figure 4.2: Energy spectrum of PG, simulated with a 160 MeV proton beam impinging on PMMA.

The detector materials have been defined with the correct chemical composition and density. The only exception is the ALPIDE electronic board which was simulated as a 100 μm Kapton layer and a 50 μm Aluminium layer, to obtain the equivalent material budget. The simulations performed exploit some customized routines in order to built an output dataset, containing the particle fundamental information as position and momentum at generation, death and crossing of different regions. Information on the particle identification has also been included, as the FLUKA particle code (to identify the particle from the Monte Carlo truth), the particle mass and charge. More details on the developed output are given in Appendix A.

4.2 Converter efficiency

The converter efficiency plays a key role in the PAPRICA chamber. In this section three different definition of efficiency will be introduced to describe the physical processes inside the converter. The study was carried out for a converter consisting of a uniform 1.5 mm thick layer of LYSO.

4.2.1 Pair production efficiency

The pair production efficiency (ϵ_{prod}) is defined as the ratio between the number of pairs produced and the number of photons incident on the front side of the converter. Figure 4.3 shows the emission spatial distribution of the pair production events. The downward trend is due to photon interactions in the medium, that reduce the fluence of gamma rays and lead to a decrease in pair production as the depth increases.

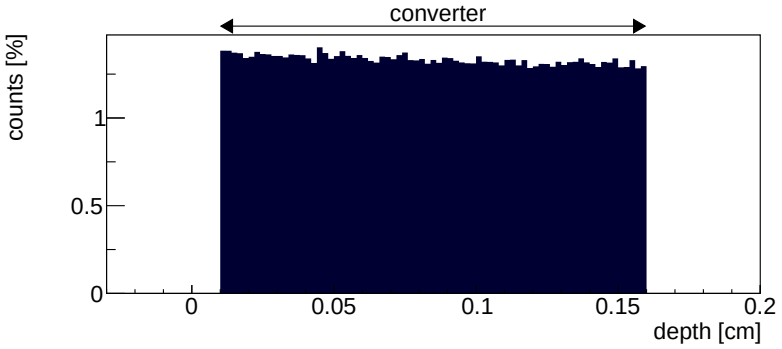

Figure 4.3: Spatial distribution of pair production events as a function of the converter depth. The converter consists of a 1.5 mm thick layer of LYSO, irradiated by a photon source with prompt gamma energy spectrum.

4.2.2 Crossing efficiency

The efficiency of converter crossing (ϵ_{cross}) is defined as the ratio between the pairs that exit from the converter and the number of pairs produced. The product between ϵ_{prod} and ϵ_{cross} is the efficiency (ϵ_{conv}) of photons conversion in electron-positron pairs, that can be detected outside the converter. Figure 4.4 shows the spatial distribution of the pair production position in the events where both positron and electron exit the converter. The particles produced at the beginning of the converter have to cross one or more hundreds of μm before leaving the converter and consequently suffer a high energy loss, with an increased probability to be absorbed.

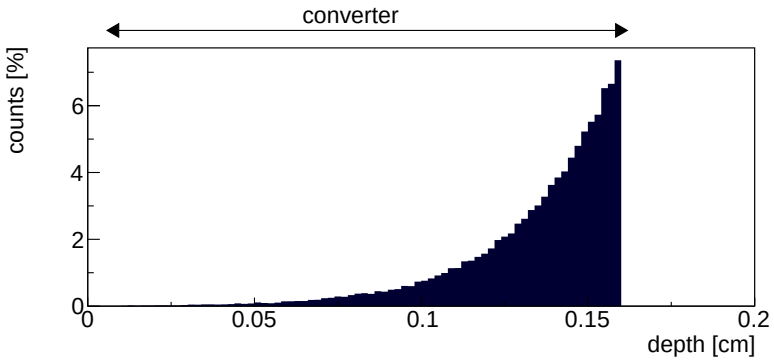

Figure 4.4: Spatial distribution of pair production events in which electron and positron exit the converter. The converter consists of 1.5 mm thick layer of LYSO, irradiated by a photon source with prompt gamma energy spectrum.

4.3 Angular resolution

The performance of the PAPRICA chamber depends on the physical processes that regulate the generation of electron-positron pair and their transmission through the detector. The dynamic of each event can be divided into four steps: pair production, electron and positron path through the converter, crossing of the tracker and absorption in the calorimeter. In this section the contribute of the first three steps to the angular resolution are presented. In the performed simulation, the distances between detectors are the minimum allowed by mechanical constraints: 0.5 cm between the converter and the first plane of ALPIDE and 2 cm between the different HICs.

4.3.1 Pair Production

The positron and electron momentum at the pair production allows to calculate the photon momentum as:

$$\mathbf{p}_{\gamma}^{pro} = \mathbf{p}_{-}^{pro} + \mathbf{p}_{+}^{pro} \tag{4.1}$$

The resulting momentum and the true value $\mathbf{p}_{\gamma}^{true}$ differ due to the nucleus recoil, which absorbs part of the photon momentum. The angle $\Delta\theta$ between the direction of the two vectors defines the angular resolution intrinsic to the pair production process. The average of its distribution, shown in Figure 4.5, is equal to $\langle\Delta\theta\rangle \pm RMS$=10.1° ± 14.4°.
The nucleus recoil is a decreasing quantity with electron and positron energy increasing, hence with photon energy increasing. This trend is well represented by the FLUKA simulation (see Figure 4.6). Gamma rays with energy range between 2-3 MeV, 4-5 MeV, 6-7 MeV lead respectively to an average angular resolution $\Delta\theta$ equal to 24.2° ± 23.0°, 11.3° ± 14.6° and 7.3° ± 11.0°.

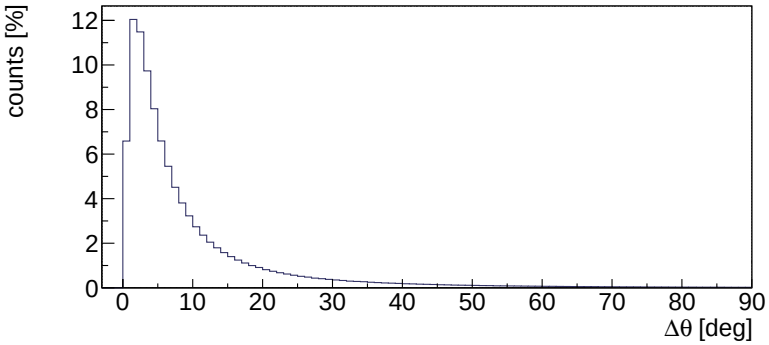

Figure 4.5: Distribution of the angle between the true PG direction and the direction reconstructed from electron and positron momentum at the pair production.

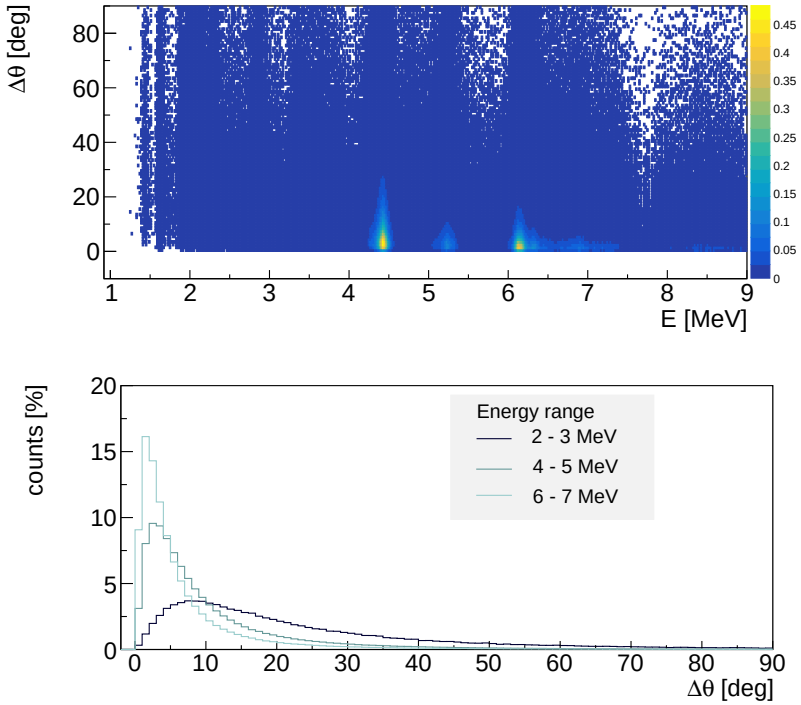

Figure 4.6: Effect of nucleus recoil on angular resolution as a function of PG energy (top). Projections for 2-3 MeV, 4-5 MeV, 6-7 MeV photon energy range (bottom).

Also the ϕ angle between electron and positron is correlated with the nucleus recoil, hence with angular resolution (see Figure 4.7). The pairs generated at large angles correspond to those events in which the nucleus recoil is greater while the pairs generated at small angles correspond to those events in which the nucleus recoil is lower and, consequently, are the most suitable pairs to reconstruct the gamma direction. Pair with electron-positron angle in 0°-10°, 20°-30° and 40°-50° range lead respectively to an average angular resolution $\Delta\theta$ equal to 3.2° ± 3.4°, 6.7° ± 7.2° and 12.1° ± 12.5°.

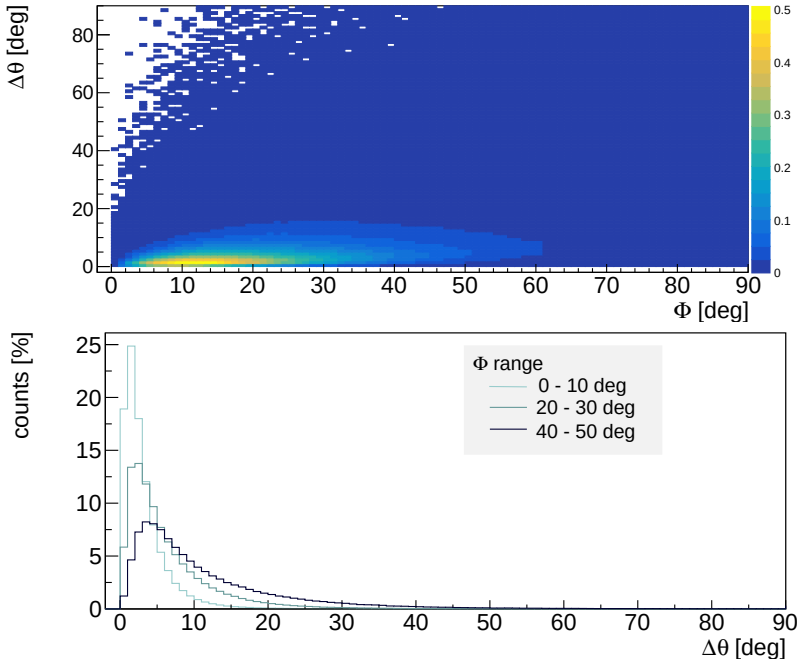

Figure 4.7: Effect of nucleus recoil on angular resolution as a function of ϕ electron-positron angle (top). Projections for 0°-10°, 20°-30° and 40°-50° ϕ range (bottom).

4.3.2 Converter crossing

The photon momentum that generated the pair can be reconstructed from the electron and positron momentum outside the converter, as

$$\mathbf{p}_{\gamma}^{conv} = \mathbf{p}_{-}^{conv} + \mathbf{p}_{+}^{conv} \tag{4.2}$$

The resulting value is affected by the nucleus recoil and the multiple scattering in the converter. To separate the two contribute, Figure 4.8 shows the angle between gamma direction reconstructed with particle momentum $\mathbf{p}_{\gamma}^{conv}$ outside the converter and gamma direction reconstructed with particle momentum at the pair production $\mathbf{p}_{\gamma}^{pro}$. The distribution average is equal to $\langle \Delta\theta \rangle \pm RMS$=24.1° ± 15.1°. The comparison between Figure 4.5 and Figure 4.8 shows that the main contribution to the degradation of the angular resolution is given by the multiple scattering. Figure 4.9 shows the dependence between the effect of multiple scattering on the angular resolution and the particle angle ϕ_z with respect to the normal axis of the converter layer. Between electron and positron angle, the greater value is chosen. The particle direction determines the path to exit the converter and, consequently, the number of scatterings that occur with electrons of the medium. An electron or a positron emitted with a large angle suffered a large change in momentum direction, leading to an incorrect estimate of the gamma direction. If ϕ_z is in the 0°-10°, 20°-30° and 40°-50° range, the average on angular resolution is respectively equal to 7.6° ± 5.9°, 13.9° ± 9.0° and 24.0° ± 12.9°.

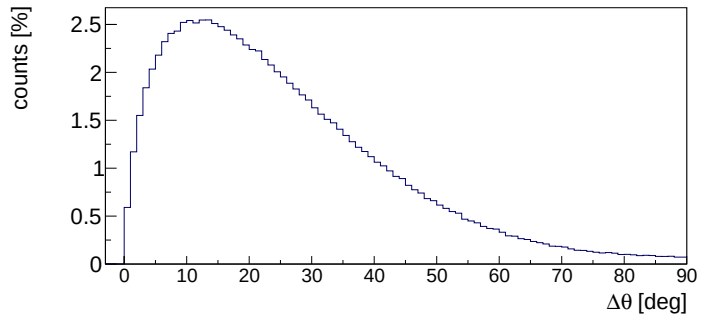

Figure 4.8: Angular difference between the PG momentum reconstructed with lepton momentum at pair production and outside the converter.

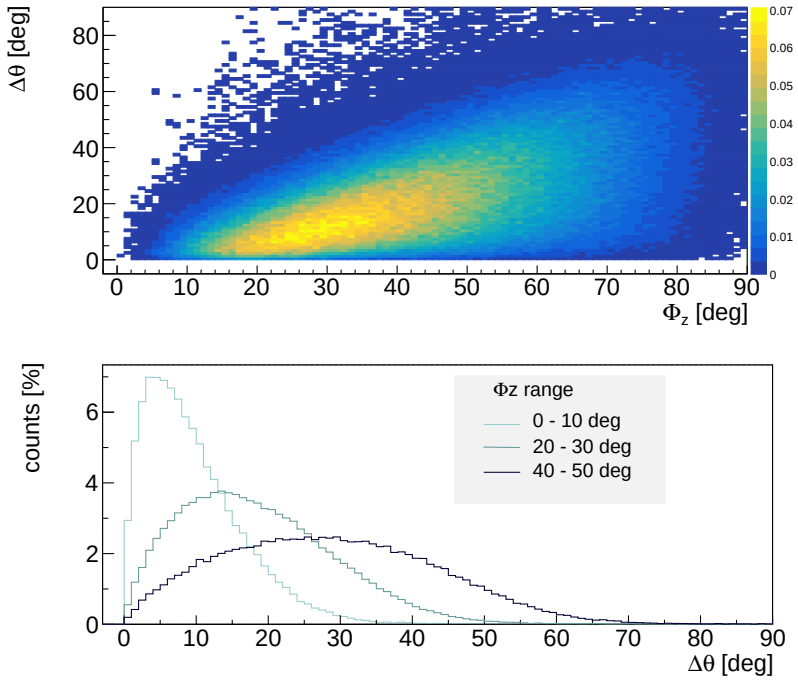

Figure 4.9: Effect of multiple scattering in the converter on angular resolution as a function of the particle angle ϕ_z (top). Projections for 0°-10°, 20°-30° and 40°-50° ϕ_z range (bottom).

4.3.3 Tracker crossing

To calculate the effect of multiple scattering in the ALPIDEs, Figure 4.10 shows the angular difference of photon direction reconstructed with the lepton momentum at the converter exit $\mathbf{p}_\gamma^{conv}$ and after the first track plane:

$$\mathbf{p}_\gamma^{hic} = \mathbf{p}_-^{hic} + \mathbf{p}_+^{hic} \tag{4.3}$$

The distribution average is equal to $\langle \Delta\theta \rangle \pm RMS$=8.4° ± 5.8°.

Figure 4.11 shows that the resolution degradation, due to multiple scattering in the ALPIDEs slowly increases with the ϕ_z angle. In 10°-20°, 30°-40° and 50°-60° ϕ_z range the distribution average is respectively equal to 7.1° ± 4.5°, 8.8° ± 5.7° and 12.0° ± 7.9°. The obtained results on the angular resolution studied at the three different levels (production, converter crossing, tracker crossing) suggest that the signal with the best angular resolution on the reconstructed photon can be selected by using the ϕ and ϕ_z variables, computed from the electron-positron track reconstruction and by measuring the reconstructed photon energy. Indeed, the chamber geometry itself will help to select the more collimated electron-positron pairs.

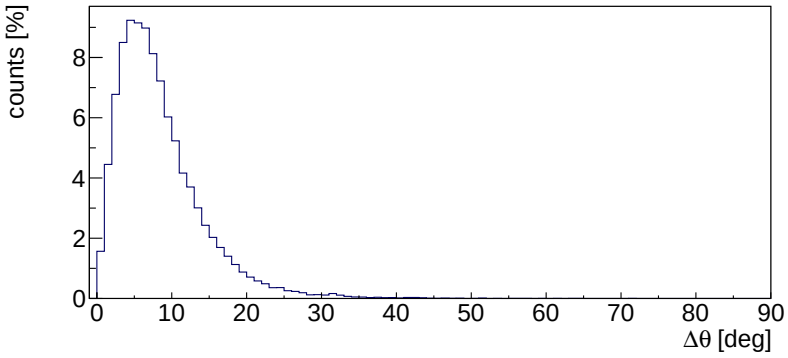

Figure 4.10: Angular difference between the PG momentum reconstructed with lepton momentum before and after the first tracker HIC.

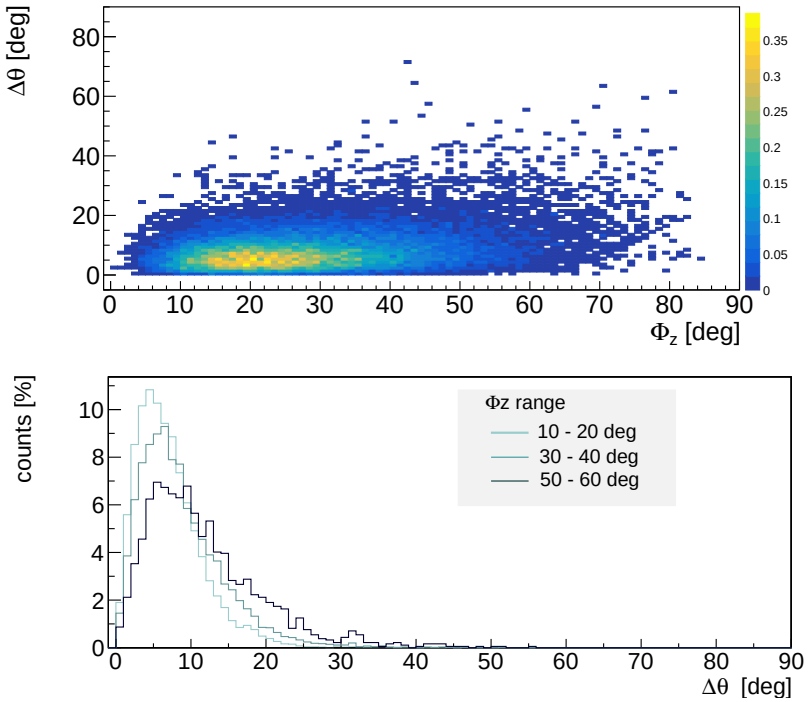

Figure 4.11: Effect of multiple scattering in the first HIC on angular resolution as a function of the particle angle ϕ_z (top). Projections for 10°-20°, 30°-40° and 50°-60° ϕ_z range (bottom).

4.4 Signal properties

This section focuses on the properties of the leptons pairs reaching the calorimeter. Figure 4.12 shows the angle between electron and positron impinging on the first HIC. The distribution mean value is 29.3° with a root mean square equal to 17.9°. Figure 4.13 presents the kinetic energy spectrum of the two leptons when crossing the second tracker HIC while Figure 4.14 shows distribution of the reduced energy ϵ, i.e. the ratio between the electron energy and the sum of leptons energies. Compared to the theoretical distribution calculated at the pair production (see Figure 3.4), the distribution obtained shows a peak in 0.5 due to the selection of the pairs leaving the converter.

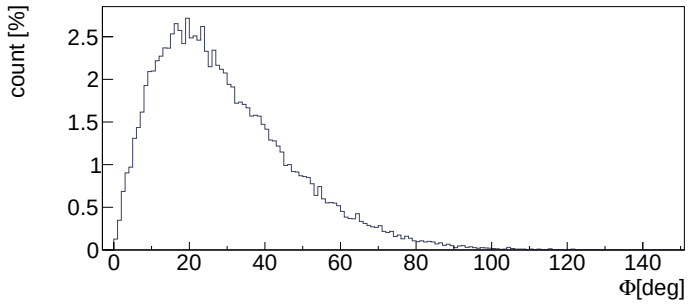

Figure 4.12: Angle between electron and positron impinging on the first HIC.

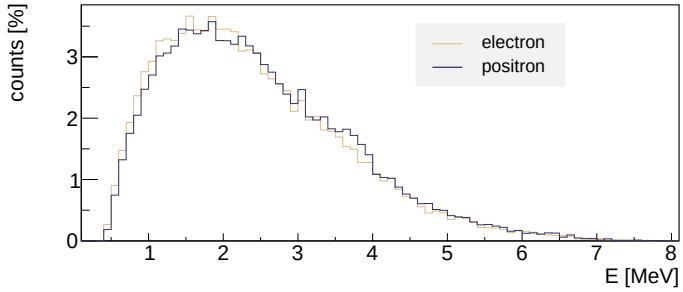

Figure 4.13: Electron and positron kinetic energy spectrum at the crossing of the first HIC.

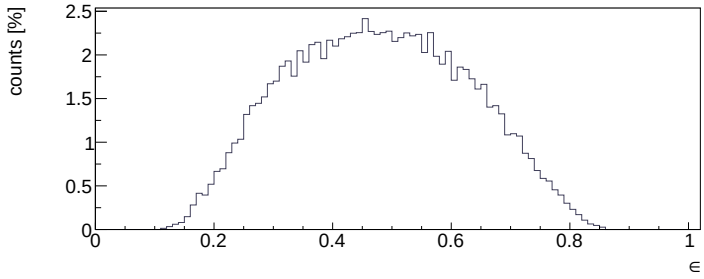

Figure 4.14: Ratio between the electron energy and the sum of leptons energies at the first HIC.

Chapter 5

Chamber optimization

This chapter presents the optimization of the PAPRICA chamber. The choice of chamber geometry and materials is driven by the search for an accurate reconstruction of the gamma ray emission point. After a brief mention of the number of photons expected in a real case scenario and the photon reconstruction method, the following sections present the choice of the converter thickness and material, the chamber performance as the distance between the tracker planes varies and the study of the calorimeter geometry.

5.1 Real case scenario

The PG yields in proton treatments have already been experimentally explored, finding as a result about $2 \cdot 10^{-5}$ PG/proton/mm/steradian [28]. The number of protons that are delivered into a target voxel in a proton PT treatment is heavily dependent on the tumour characteristics (extension and depth). In the distal region, nearby the tissues that have to be spared from unnecessary radiation, typical values for the number of protons are 10^8 for each pencil beam [19].

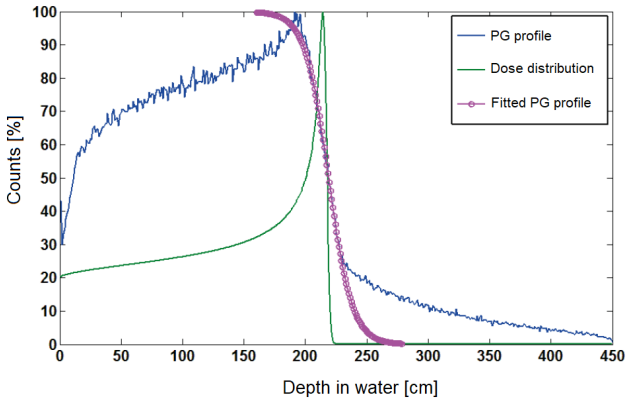

Figure 5.1: Bragg curve (green), prompt gamma profile (blue) and a fit through the fall-off region of the prompt gamma profile (violet) for a 180 MeV proton pencil beam in water [54].

The spatial region of the PG emission profile interesting for the range monitoring is the distal fall-off, which stretches few cm (see Figure 5.1). Assuming to sum the statistic of 30 pencil beams and to reconstruct 5 cm of the emission profile, the number of photons per steradian is equal to $3 \cdot 10^6$. The PAPRICA converter covers a solid angle of 0.11 sr, however, in a real scenario several chambers can be placed side by side to cover 1 steradian.

5.2 Vertex reconstruction

In order to reconstruct the prompt gamma emission point, the photon momentum has been calculated as the sum of leptons momentum at the second HIC, the vertex of the pair production has been estimated projecting the electron and positron direction from the first HIC towards the converter and, finally, the direction of the photon has been projected to the source plane (see Section 3.3). Only pairs which cross the entire tracker were considered. The vertex of pair production has been calculated as the point of closest approach of the lepton trajectories. Figure 5.2 shows the distance between the calculated vertex and the true pair production point, on the three axis. The simulations were performed with LYSO 1.5 mm thick converter and the minimum distance between the detectors, allowed by the geometrical constraints: 0.5 cm between the converter and the first plane of ALPIDE and 2 cm between the different HICs. The difference between the X and Y axes of the converter is due to the chamber asymmetry. On the X-axis the angular acceptance is larger and consequently higher resolution pairs are detected with respect to the Y-axis. The vertex reconstruction on the longitudinal Z-axis is characterized by a systematic shift.

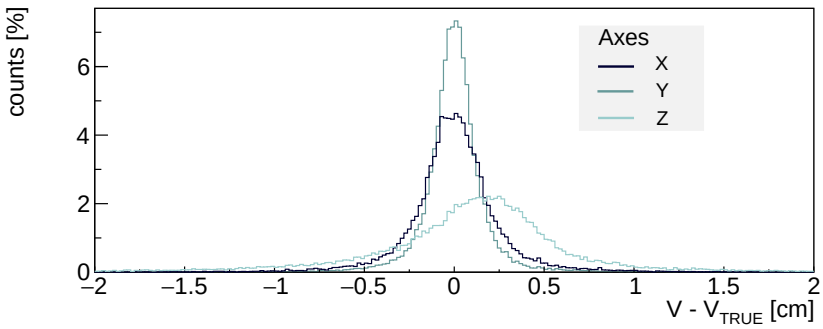

Figure 5.2: Resolution of pair production vertex on the three axis, calculated from lepton momentum at the crossing of the second HIC.

5.3 Converter optimization

The first step in the optimization of the PAPRICA chamber is the choice of converter material and thickness. Material and thickness choice is a trade-off between pair production and multiple scattering cross section. The first parameter determines the efficiency of photon conversion in a pair positron-electron, while the second leads to a reduction of particle transmitted outside the converter and to an information loss about the particle momentum. The material and the different thickness studied in the simulations are summarized in Table 5.1. The greatest thickness for each material was chosen on the basis of a preliminary analysis that studied the maximum thickness that can be crossed by the leptons of the pair. The simulations were performed with the minimum distance between the detectors, allowed by the geometrical constraints.

Material	Symbol	Thickness
Plastic	BC404	10 mm
Lutetium-Yttrium OxyorthoSilicate	LYSO	0.05 mm, 0.1 mm, 1,5 mm
Tungsten	W	0.05 mm, 0.1 mm, 0,5 mm
Lead	Pb	0.05 mm, 0.1 mm, 1,0 mm

Table 5.1: Material and thickness studied for the converter optimization.

5.3.1 Efficiency

Table 5.2 shows the efficiency values (defined in Section 4.2) for each material and thickness studied.

Material	Thickness [mm]	$\epsilon_{prod}[10^{-2}]$	$\epsilon_{cross}[10^{-1}]$	$\epsilon_{conv}[10^{-3}]$	$\epsilon_{tot}[10^{-5}]$
BC404	10.00	1.6	3.4	0.6	3.2
LYSO	0.05	0.4	9.5	0.4	3.0
	0.10	0.9	9.0	0.8	4.9
	1.50	12.8	1.9	2.4	10.1
W	0.05	1.5	8.6	1.3	7.1
	0.10	3.3	7.3	2.2	9.1
	0.50	14.7	2.0	3.0	12.1
Pb	0.05	1.0	9.2	0.9	5.5
	0.10	1.9	8.4	1.6	8.0
	1.00	18.6	1.6	3.1	12.3

Table 5.2: Efficiency of the studied converters, ordered by increasing atomic number and thickness.

ϵ_{pair} and ϵ_{conv} increase with the thickness, atomic number and density of the material, while ϵ_{cross} follows the opposite trend. In the last column the total efficiency (ϵ_{tot}), defined as the ratio between the incident photons on the converter and the number of pairs that cross all the tracker planes, is shown. This quantity is referred to the geometry of the tracker with the minimal inter-plane distance allowed by the mechanical constraints.

5.3.2 Resolution

The momentum of the photon, calculated as the sum of the momentum of the leptons, was projected from the vertex to the plane of the source. The distribution of the reconstructed points on the plane determines the spatial resolution of the chamber. Figure 5.3 shows the distribution obtained for different thicknesses of the LYSO converters.

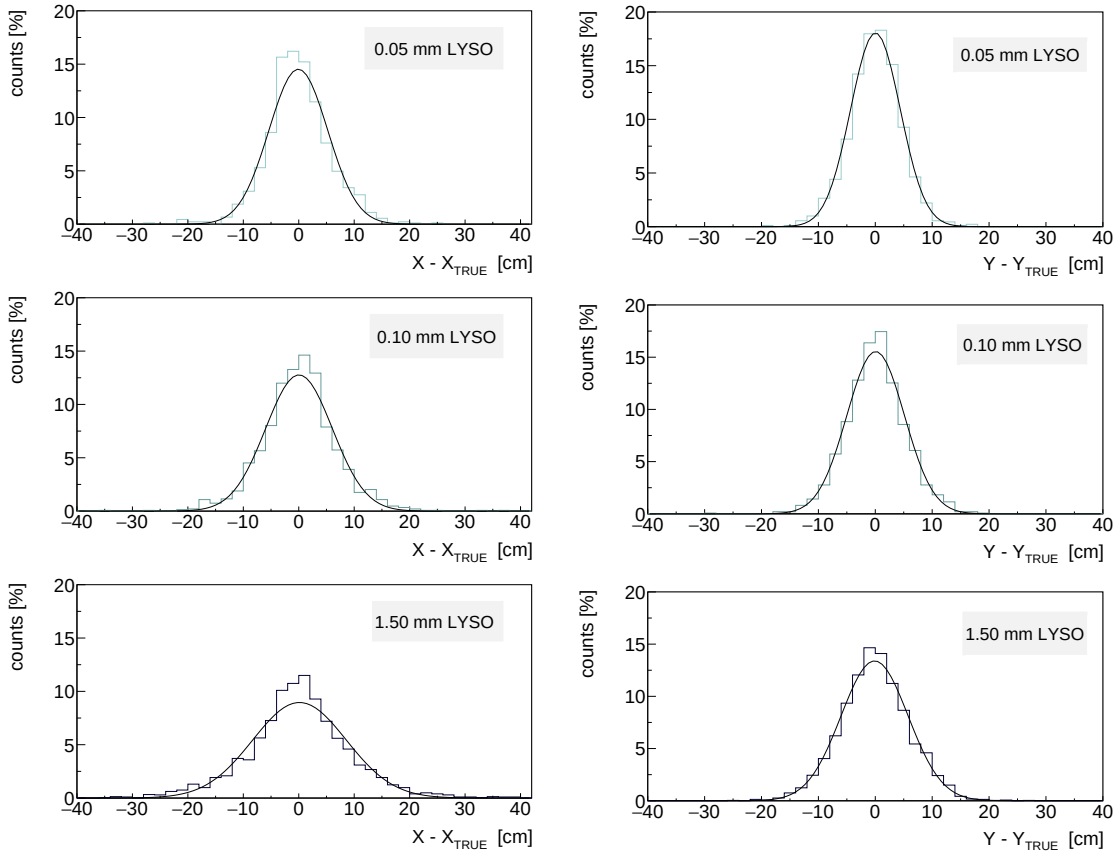

Figure 5.3: Distribution of the reconstructed emission points, relative to the real source, for different thicknesses of the LYSO converter on X (left) and Y (right) axes. From the top 0.05 mm, 0.1 mm and 1.5 mm thickness. A Gaussian fit was carried out for each distribution.

For the other materials proposed, similar distributions have been obtained and a Gaussian fit has been made for each of them. In Table 5.3 are reported the standard deviation σ and standard error δ on each axis of the source plane for the different converter material and thicknesses.

The standard deviation represents the spatial resolution of the single reconstructed event, and it increases with thickness, atomic number and density of the materials. The standard error has been calculated as:

$$\delta = \frac{\sigma}{\sqrt{\epsilon_{tot} \cdot N}} \tag{5.1}$$

where N is the photon number expected in a real case scenario for a converter surface that cover 1 steradian ($3 \cdot 10^6$ photons). The standard error represents the chamber resolution on the reconstructed mean value. The plastic converter returns the worst resolution value due to the low number of pair produced. For the LYSO converter the resolution increases with the thickness of the converter. For the heavier elements, W and Pb, the resolution improves with the thickness on the Y axis and fluctuates, without a recognizable trend, on the X axis. The comparison between the different materials and thicknesses shows that the best spatial resolution is achieved on Y axis in 1 mm of Lead or in 0.5 mm of Tungsten. However 1.5 mm LYSO spatial resolution is equal to 3.3 mm, with a worsening resolution within 10%. For the advantage of an active converter, a LYSO layer has been chosen, consisting of an array of 133 fibers 1.5 x 1.5 x 50 mm^3 [55], placed side by side, resulting in a total surface of 20 x 5 cm^2 and a thickness of 1.5 mm.

Material	Thickness [mm]	σ_x [cm]	σ_x [cm]	δ_x [mm]	δ_y [mm]
BC404	10.00	5.6	4.7	5.7	4.8
LYSO	0.05	5.0	4.2	5.3	4.4
	0.10	5.7	4.8	4.7	4.0
	1.50	8.2	5.7	4.7	3.3
W	0.05	6.5	5.2	4.5	3.5
	0.10	7.7	5.5	4.7	3.3
	0.50	8.9	6.0	4.7	3.1
Pb	0.05	5.9	4.8	4.6	3.8
	0.10	6.7	5.2	4.3	3.4
	1.00	8.8	6.1	4.6	3.1

Table 5.3: Spatial resolution of photon emission point reconstruction for different material and thickness. σ is the resolution of a single event while δ is the resolution on the reconstructed mean value in a real case scenario.

5.4 Tracker optimization

The choice of the distance between the tracker planes must take into account the efficiency of the chamber, the uncertainty in particle tracking due to the finite pixel size, and the selection of events. Angular acceptance, and consequently geometrical efficiency, decreases as the distance between detectors increases. The spatial resolution on the reconstructed position at the converter plane, i.e. the pair production vertex, depends on the number of tracker planes N, the tracker length L, the intrinsic tracker resolution σ and the distance between the tracker half and the vertex plane z_c (see Figure 5.4):

$$\sigma_V^2 = \frac{\sigma^2}{N+1}\left(1 + \frac{12}{N+2}\frac{z_c^2}{L^2}\right) \tag{5.2}$$

The intrinsic resolution of the tracker is $\sigma \sim 30\mu\text{m}/\sqrt{12}$ where 30 μm is the pixel side. Considering 3 planes, with a distance of 4 cm between the first and the last and 2.5 cm between the second and the surface of the converter, the resolution on the vertex is about 6 μm, negligible compared to the error due to multiple scattering, as shown in Section 5.2. In the choice of the distance between the HICs, the event selection has to be considered.

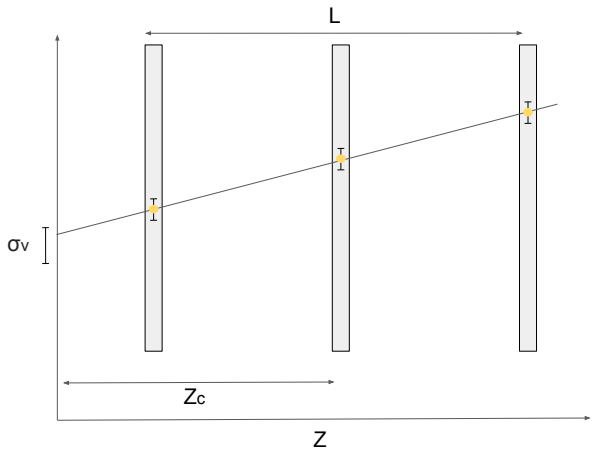

Figure 5.4: Tracker sketch. The spatial resolution on vertex reconstruction σ_V depends on the number of tracker planes N, the tracker length L, the intrinsic tracker resolution σ and the distance between the tracker half and the vertex plane z_c

Due to the finite angular acceptance, the pairs emitted at small angles with respect to the direction normal to the detectors are more likely to be tracked up to the calorimeter. These pairs are associated with events with better angular resolution and therefore the distance between the planes allows to reduce the error on the single reconstructed event. Three simulations have been performed with the LYSO converter chosen in the previous section and a distance between two successive planes of ALPIDEs equal to 2 cm, 4 cm and 8 cm.

5.4.1 Efficiency

For each configuration, Table 5.4 shows the tracker efficiency ($\epsilon_{tracker}$), defined as the ratio between number of pairs that exit the converter and the number of pairs that cross the three HICs. ϵ_{tot} introduced in the previous section is the total efficiency of the chamber.

Hic distance	$\epsilon_{tracker}$	ϵ_{tot}
2 cm	4e-02	1.0e-04
4 cm	1e-02	2.7e-05
8 cm	2e-03	4.2e-06

Table 5.4: Tracker and total efficiency for different distances between HICs.

5.4.2 Resolution

Figure 5.5 compares the spatial resolution in photon emission point reconstruction for the three geometry of the tracker.

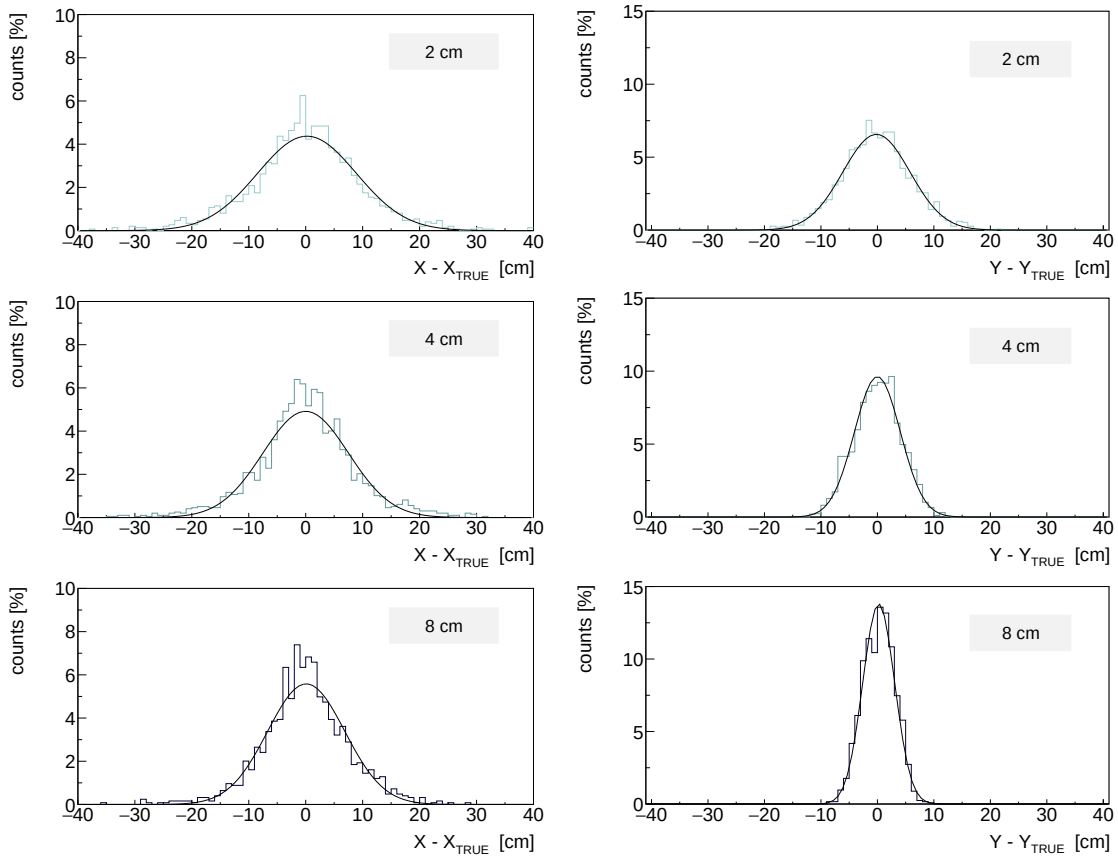

Figure 5.5: Distribution of the reconstructed emission points, relative to the real source, for different distances between the HICs, from the top: 2 cm, 4 cm e 8 cm.

For each configuration, the second and the third column of Table 5.5 show the standard deviation of the spatial distribution obtained on the source plane, with respect to the X and Y axes. In the last two columns the standard error, found as described by Equation 5.1, is shown.

Hic distance	σ_X[cm]	σ_Y[cm]	δ_X[mm]	δ_Y[mm]
2 cm	8.3	5.8	4.8	3.3
4 cm	7.1	4.1	7.9	4.6
8 cm	6.4	2.9	18.0	8.2

Table 5.5: Spatial resolution of photon emission point reconstruction for different distances between HICs. σ is the resolution of a single event while δ is the standard error in a real case scenario.

The configuration that returns the best estimate of the source position is the one that minimizes the distance between the ALPIDEs increasing the statistics. The event selection is not sufficient to compensate for the loss of pairs.

5.4.3 Photon energy selection

Figure 5.6 compares the photon spectra that generate the tracked pairs. The ratio between the 4.4 MeV and 6 MeV peaks decreases by increasing the inter-planes distance. In fact, the angular acceptance of the chamber sets an energy cut-off due to the dependence of the lepton angle by the photon energy. The choice of the first configuration (2 cm) therefore allows to lose fewer events due to 4.4 MeV photons, which are the most related to the Bragg peak.

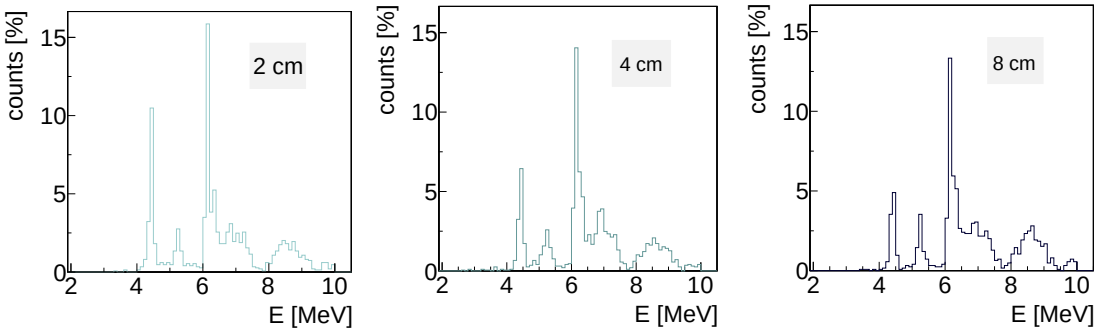

Figure 5.6: Photon spectra that generate the tracked pairs for different distances between HICs, from left : 2 cm, 4 cm, 8 cm.

5.5 Calorimeter geometry

To study the calorimeter geometry, a simulation has been performed with a non-pixelated detector with a surface area of 30 x 30 cm^2 and a thickness of 4 cm. The tracker geometry is the one optimized in the previous section. Figure 5.7 shows the position where electron and positron cross the three tracker planes and impinge on the surface of the calorimeter. About 98% of the particles can be detected by a detector of 5 x 21 cm^2 surface.

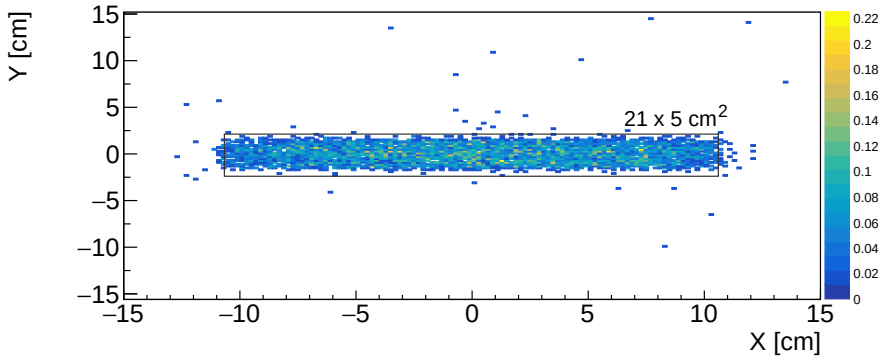

Figure 5.7: X-Y map of the points where the leptons of the pair cross the 30 x 30 cm^2 calorimeter, simulated with the optimized tracker geometry, and sketch of a calorimeter of 5 x 21 cm^2 surface

The 90% of electrons and positrons that reach the calorimeter stops inside the plastic, while the 10% is backscattered by the front face. This percentage is independent on the surface dimension and depends only on the calorimeter material. Figure 5.8 shows the position on Y - Z axes where the leptons stop in the calorimeter. A 4 cm plastic thickness is enough to absorb all the pairs that reach the calorimeter.

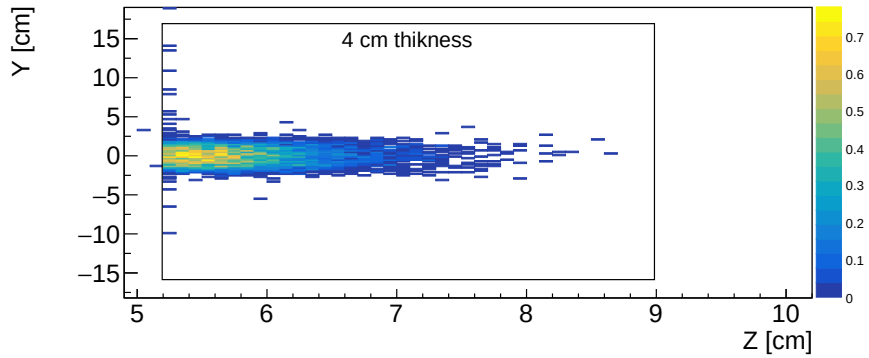

Figure 5.8: Y-Z map of the points where the leptons of the pair stop in the 4 cm thick calorimeter.

The calorimeter must be divided into pixels to detect electron and positron separately. In order to determine the maximum pixel size, the distance between the electron and positron coordinates at the entrance in the calorimeter was calculated (see Figure 5.9). In 95% of the events the distance is greater than 0.5 cm. Based on the obtained results, the

proposed calorimeter is composed of a matrix of 32 x 8 pixels measuring 0.6 x 0.6 x 4 cm^3 each, for a total area of 19.2 x 4.8 cm^2.

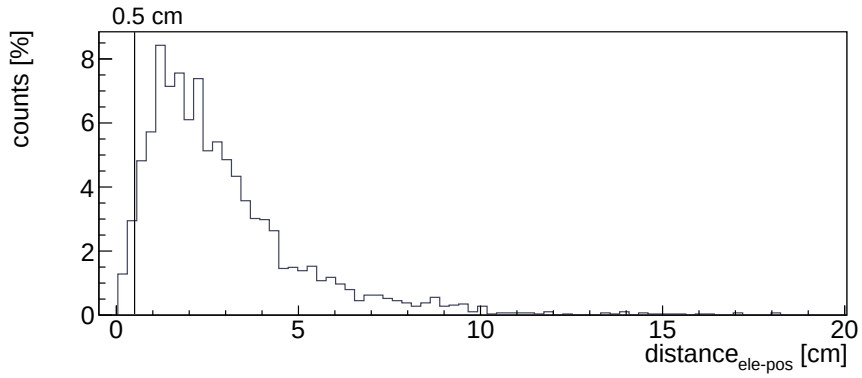

Figure 5.9: Distance between the points where electron and positron enter the calorimeter, simulated with the optimized tracker geometry.

5.6 Final design

The study of the chamber optimization led to the choice of the final geometry. The converter consist an array of 133 LYSO fibers 1.5 x 1.5 x 50 mm^3 [55], placed side by side, resulting in a total surface of 20 x 5 cm^2 and a thickness of 1.5 mm. In addition, a cover of EJ212 reflective paint has been hypothesized to separate the light produced by each fiber. The tracker consists of three HIC 3 x 20 cm^2 of ALPIDEs. The planes will be spaced 2 cm apart and 5 mm from the converter and the calorimeter. The calorimeter is composed of a matrix of 32 x 8 plastic pixels [50], measuring 0.6 x 0.6 x 4 cm^3, for a total area of 19.2 x 4.8 cm^2. The final performances on the reconstruction of a single event are summarized in Table 5.6, assuming to reconstruct the events starting from the momentum of the leptons in the second plane of ALPIDEs.

Total efficiency (ϵ_{tot})	$1.0 \cdot 10^{-4}$
Angular resolution ($\Delta\theta$)	$16.9° \pm 10.6°$
Spatial resolution X-axis (σ_x)	8.3 cm
Spatial resolution Y-axis (σ_y)	5.8 cm
Resolution on mean value X-axis (σ_x)	4.8 mm
Resolution on mean value Y-axis (σ_x)	3.3 mm

Table 5.6: Chamber performance on the gamma ray reconstruction.

Chapter 6

Prompt gamma reconstruction

In order to optimize the PAPRICA geometry, the results of the previous chapters are obtained from the knowledge of the particle position and momentum at the instant of production or when the particle crosses two different regions, i.e. accessing the Monte Carlo truth information. On the other hand, in order to evaluate the PAPRICA performances, the FLUKA simulation allows to access variables equivalent to the experimental ones, thanks to the developed user routines (see Appendix A). In this chapter the photon reconstruction algorithm is presented, using the same simulation described in Section 4.1 and with the optimized chamber geometry described in Section 5.6. The algorithm basis is the definition of *hit*, the energy release of one or more particles in an active region as LYSO fibers, ALPIDE or calorimeter pixels. The energy threshold that will be set in real detectors is not considered while the detectors energy and spatial resolution are taken into account. In the ALPIDEs and in the calorimeter the interaction point of the particles is defined as the center of the crossed pixel area, introducing an error equal to the pixel side divided by $\sqrt{12}$, i.e. the standard deviation of a flat distribution. Figure 6.1 shows the distribution of the number of hits per event in a plane of ALPIDE and in the calorimeter. The analysis carried out in this chapter is limited to events in which a pair generated in the converter crosses the planes of the tracker and reaches the calorimeter. The simplest case is considered, in which there are two hits for each plane of the tracker, one from the electron and one from the positron. These cases are the 90% of the events in which the pair reaches the calorimeter. To reconstruct the dynamic of the event the hits in the ALPIDEs and in the calorimeter must be associated to a track, in order to determine the direction and the momentum of the pair. The reconstruction algorithm, as illustrated in Section 3.3, can therefore be applied to reconstruct the photon direction and its emission position. The purpose of this chapter is to illustrate each step of the developed reconstruction algorithm, using the experimental-like variables. Final results on the PAPRICA performances are reported in the last section.

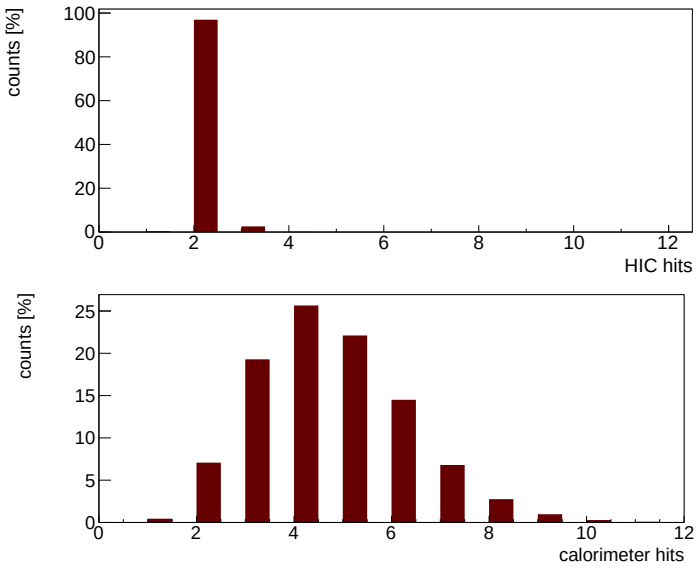

Figure 6.1: Number of hits per event in an ALPIDE HIC (top) and in the calorimeter (bottom). The events considered are those in which an electron-positron pair, generated in the converter, crosses the tracker and reaches the calorimeter.

6.1 Identification of tracks

The first step in particle tracking is to associate each hit in the ALPIDEs to a track. For this purpose, all possible triplets formed by one hit per plane are considered (see Figure 6.2).

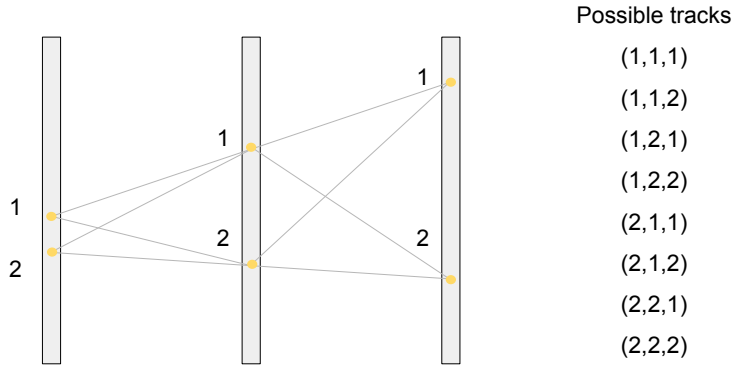

Figure 6.2: The eight possible tracks that can be defined in the events with two hits for each plane of the ALPIDEs.

6.1.1 Chi-squared test

If three hits were generated from the same particle they lie approximately on a straight line. To check which triplets meet this condition, a linear fit can be made for each of them. The fit is performed on the two X and Y axes with respect to the Z axis normal to detectors. The result is two straight lines equations for each track:

$$\begin{aligned} x &= m_x z - q_x \\ y &= m_y z - q_y \end{aligned} \tag{6.1}$$

Each fit is characterized by a χ^2 value which determines how accurately the linear fit describes the position of the three points in space. The χ^2 value is defined as:

$$\chi^2 = \sum_{i=1}^{nHit=3} \frac{(x_i - m_x z_i - q_x)^2 + (y_i - m_y z_i - q_y)^2}{3} \tag{6.2}$$

6.1.2 Track selection

Each hit can only be associated with one track, and when a triplet is chosen the second triplet is automatically defined. The different combinations of triplets that have no hits in common are four. To choose the combination that identifies the straight trajectories, the χ^2 values of the two triplets were added together, and the combination with the lower value has been chosen. Two examples are reported in Table 6.1.

Event 1

Track I			χ^2	Track II			χ^2	χ^2_{TOT}
1	**1**	**1**	0.01	**2**	**2**	**2**	0.01	0.02
1	1	2	0.26	2	2	1	0.19	0.45
1	2	1	0.23	2	1	2	0.31	0.54
2	1	1	0.01	1	2	2	0.02	0.03

Event 2

Track I			χ^2	Track II			χ^2	χ^2_{TOT}
1	1	1	0.07	2	2	2	0.13	0.20
1	1	2	0.22	2	2	1	0.19	0.41
1	2	1	0.22	2	1	2	0.24	0.46
2	**1**	**1**	0.01	**1**	**2**	**2**	0.01	0.02

Table 6.1: Two example of track selection. For each track the possible triplets of hits and their χ^2 are reported. The indexes 1 and 2 represent the particle that generated the hit. The combination of chosen tracks minimizing the χ^2 sum are written in bold.

For each event, hits corresponding to an electron or a positron can be correctly assigned to the e^+ and e^- tracks or can be swapped in a tracker plane. Four cases are defined:

- **case 0** hits are correctly assigned to the electron and positron tracks
- **case 1** hits in the first plane are swapped
- **case 2** hits in the second plane are swapped
- **case 3** hits in the third plane are swapped.

Figure 6.3 shows the fraction of events in which the above cases occur. In the 25% of the events the two hits are exchanged in the first plane, due to the small distance between the lepton trajectories. Between planes the trajectories widen and the probability of exchanging the two hits decreases. The number of events in which hits are erroneously assigned in the second or third plane of ALPIDEs is respectively 1.5% and 3%.

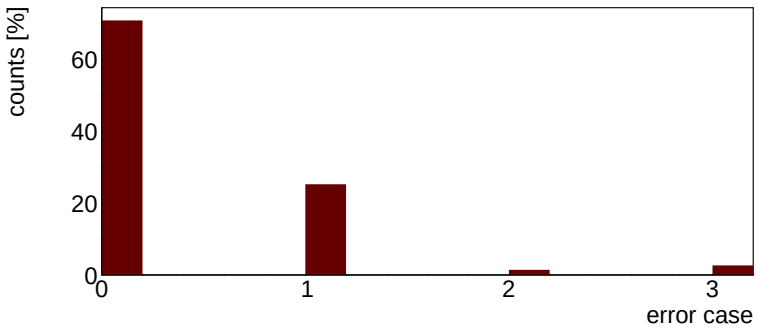

Figure 6.3: Fraction of events in which the hits are correctly assigned to the tracks (0) or a swap has occurred in the first (1), second (2) or third (3) tracker plane.

Figure 6.4 shows the reconstruction of the vertex on the Z axis, for the different error cases. The vertex is calculated, as described in Section 3.3, assuming as track direction the vector that joins the hits of the first and second tracker plane. This choice minimizes the effect of multiple scattering in the ALPIDEs on the vertex reconstruction.

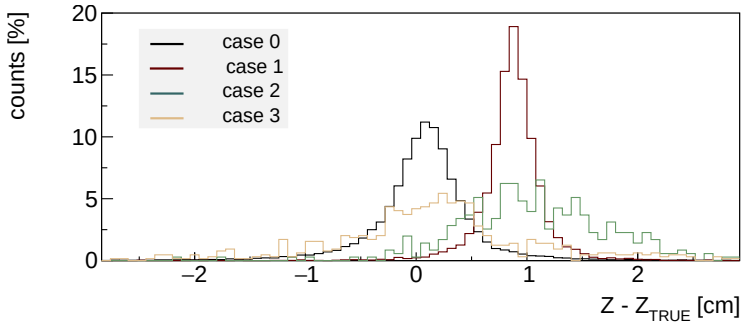

Figure 6.4: Accuracy in vertex reconstruction on the Z-axis, in different error cases.

An exchange of hits in the first or second plane of the tracker leads to a vertex reconstructed about 1 cm after the converter, i.e. beyond the first ALPIDE plane (placed 0.5 cm from the converter); almost no effect can be valued for the case 3. To correct the HIT exchange in the first tracker plane, when the Z coordinate of the vertex is greater than 6 mm, the two HITs are reversed. The percentage of case 1 thus falls from 25% to 10%, and the percentage of case 0 increases to 85%, as shown in Figure 6.5.

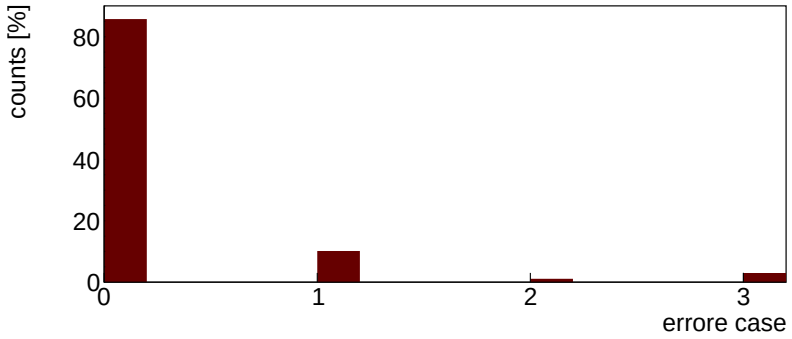

Figure 6.5: Fraction of events in which the hits are correctly assigned to the tracks (0) or a swap has occurred in the first (1), second (2) or third (3) tracker plane, with the correction based on vertex position.

6.2 Backtracking

6.2.1 Energy measurement

After detecting two tracks in the ALPIDEs, one or more activated pixels of the calorimeter must be associated to each track in order to estimate the leptons momentum and reconstruct the photon direction. To this aim, the vector that joins the hits of the second and third plane is projected on the surface of the calorimeter. Figure 6.6 shows the distance between the projection on calorimeter of an electron or positron track and the center of the pixel area crossed by the same particle.

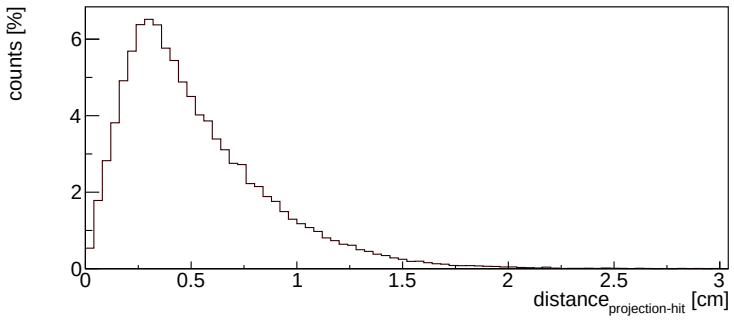

Figure 6.6: Distance between the track projection on the calorimeter surface and the center of the area of the pixels crossed by the particle.

This distribution allows to define a distance cutoff $d_{cutoff} = 1.5$ cm between the projection of a track and the pixels that can be associated to it. To assign the pixels with an energy deposition to a track, for each hit a circle is drawn around the pixel center with radius d_{cutoff}, as shown in Figure 6.7. If there is a projection of a track inside the circle the pixel is associated to it. If there are several projections the pixel is associated to the track with the closest projection.

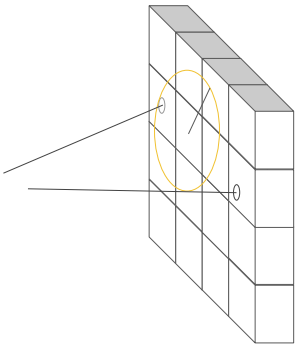

Figure 6.7: Projection of the tracks on the calorimeter, draw of a circular area of 1.5 cm radius around each activated pixel and assignment of the pixel energy to the track with the closest projection inside the area.

The energy values of the pixels associated with the same track are added together and a Gaussian error equal to 5% is added in order to take into account the calorimeter resolution. Figure 6.8 shows the relative error in energy estimation, calculated as:

$$\frac{\sigma_E}{E_{teo}} = \frac{E_{teo} - E_{dep}}{E_{teo}} \tag{6.3}$$

where E_{dep} is the estimated energy and E_{teo} the theoretical value. E_{teo} is assumed equal to the energy at the calorimeter surface of the particle that generated the third hit of the track considered. The average of the relative error is equal to 0.14 with a RMS equal to 0.24.

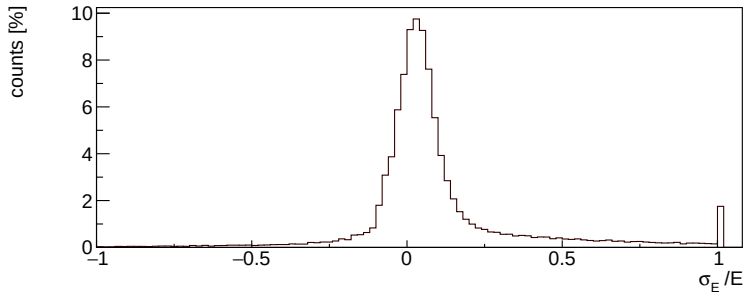

Figure 6.8: Relative error in the calculation of particle energy by assigning the energy release in the calorimeter to the tracks.

6.2.2 Lepton momentum estimate

After identifying the tracks and estimating the energy released in the calorimeter, the photon direction and the point of emission can be reconstructed. In order to evaluate the importance of the leptons energy measurement and give an estimate of the required calorimeter energy resolution three methods are studied where the lepton momentum magnitude is calculated as:

- momentum magnitude at the crossing of the calorimeter surface (**True**)
- momentum magnitude from energy release in the calorimeter (**Calo**)
- unit magnitude (**Unit**).

The first case exploits the Monte Carlo information, as it was done in Chapter 5. In the second method the momentum magnitude is obtained as:

$$p = \sqrt{(E + m_0)^2 - m_0^2} \tag{6.4}$$

where E is the energy released in the calorimeter and associated to the track as described in the previous section. Finally, the leptons momentum magnitude is chosen equal to 1. Figure 6.9 shows the spatial resolution on the emission point of the prompt gamma, obtained with the three different methods for the leptons momentum calculation. Averages and standard deviations of distributions are reported in Table 6.2: the error on the measurement of the lepton momentum magnitude does not affect significantly the calculation of the photon direction. However the presence of the calorimeter in the PAPRICA geometry is still mandatory to trigger the data acquisition and for the event selection. Further studies are foreseen on this topic, but are not being covered by this thesis.

Method	σ_X [cm]	σ_Y [cm]
True	8.5	5.9
Calo	8.6	6.0
Unit	9.0	6.1

Table 6.2: Spatial resolution on the reconstructed photon using different methods of particle momentum magnitude calculation.

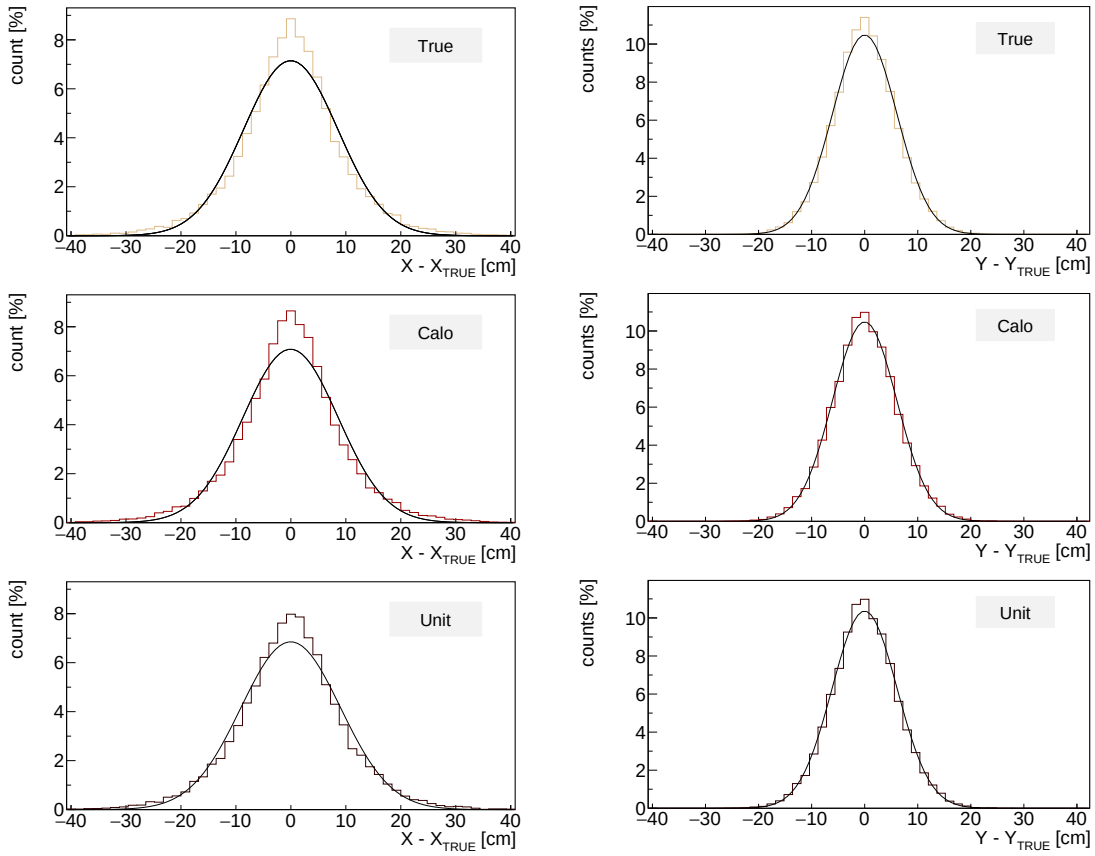

Figure 6.9: Distribution of the reconstructed emission points, relative to the real source, on X axis (left) and on Y axis (right) for different methods of calculation of particle momentum magnitude.

6.3 Results

Table 6.3 shows the final performance of the optimized chamber by reconstructing the events from the hits in the tracker planes and the energy released by the positron and electron in the calorimeter. The spatial resolution on the single reconstructed photon is about 6 cm along the Y direction and 8 cm along the X direction. Considering the number of expected pairs in a clinical scenario and the backtracking efficiency obtained in Section 5.6, the resolution on the spatial distribution average of the reconstructed photons is about 3 mm and 5 mm respectively for the X and Y-axis, close to the accuracy required in the measurement of the primary beam range in the treatment of particle therapy. The performances obtained with the data-like reconstruction algorithm are very similar to those obtained with the position and momentum given by the Monte Carlo simulation, as described in Section 5.6. Although very simple, the proposed algorithm gives good results and the resolution achievable by the camera depends mainly on the intrinsic limits. A fundamental step will be to apply and develop the algorithm in a simulation that takes into account the presence of the background.

Total efficiency (ϵ_{tot})	$1.0 \cdot 10^{-4}$
Angular resolution ($\Delta\theta$)	$17.3^\circ \pm 10.5^\circ$
Spatial resolution X-axis (σ_x)	8.3 cm
Spatial resolution Y-axis (σ_y)	5.8 cm
Resolution on mean value X-axis (σ_x)	4.8 mm
Resolution on mean value Y-axis (σ_x)	3.3 mm

Table 6.3: Chamber performance on the prompt gamma ray reconstruction.

Conclusion

The project PAPRICA (PAir PRoduction Imaging ChAmber), started from the collaboration between the Istituto Nazionale di Fisica Nucleare and the Università Sapienza di Roma, proposes an innovative method for the range monitoring in tumor treatments by means of particle therapy. The proposed system is based on the detection of the prompt gamma emitted by the de-excitation of the nuclei involved in the nuclear interaction between the beam and the patient tissues, exploiting the photon pair production mechanism. The measurement of the two generated leptons (electron and positron) allows to reconstruct the direction of the incident photon and, subsequently, the spatial distribution of the emitted prompt gamma rays, which is correlated to the beam range within the patient. The PAPRICA detector consists of a converter, where the pair production takes place, a three planes tracker, based on Silicon pixelated detectors, to reconstruct the vertex of production of the pair and a calorimeter to measure the kinetic energy of the leptons.
This thesis represents the first feasibility study of the PAPRICA chamber, using Monte Carlo simulations developed with the FLUKA code. The first part of this work showed that the recoil of the nucleus involved in the pair production introduces an intrinsic limit to the angular resolution on the reconstructed photon. However the main factor in degrading the angular resolution achievable with PAPRICA is the multiple scattering of the leptons in the path to exit the converter. A thin converter reduces the effect of multiple scattering but on the other hand significantly reduces the number of pairs produced. In the second part of the thesis, the geometry of the chamber has been optimized, in particular the thickness and material of the converter, the distance between the planes of the tracker and the size of the calorimeter. The results obtained led to the choice of a 1.5 mm thick converter consisting of 133 LYSO fibres, a scintillating crystal with a high atomic number (Z=66) to maximise the pair production cross-section (proportional to Z^2). The choice of an active material will allow to select the events by means of an acquisition trigger that foresees the temporal coincidence of the signals between the converter and the calorimeter. In optimizing the distance between the tracker planes, the best results have been obtained for the minimum distance allowed by the constraints of the detector mechanics and electronics. The optimized calorimeter consists of a 32 x 8 matrix of plastic scintillator rods each measuring 0.6 x 0.6 x 4 cm^3. The low atomic number of the plastic

reduces the backscattering effect of the leptons from the calorimeter, while the thickness of the rods allows a complete absorption of the incident leptons. In the last part of this thesis work an algorithm for the reconstruction of the photon direction, based on the signals generated by the particles in the tracker and calorimeter, has been developed and verified. The spatial resolution on the reconstructed prompt gamma ray for the optimized chamber geometry is 6 cm along Y direction and 8 cm along the X direction on the single event. Considering the number of expected pairs in a clinical scenario, the expected resolution on the spatial distribution of the reconstructed photons is $\sim$ 3-5 mm. The results obtained showed that the resolution achievable by the PAPRICA detector is compatible with the accuracy required in measuring the primary beam range in particle therapy treatments. The work carried out in this thesis represents the first milestone of the PAPRICA project, which will be continued by the relative INFN - Sapienza collaboration for the next two years.

Appendix A

FLUKA output

The FLUKA output has been developed ad-hoc by means of user routines in order to score the reported quantities. For each event the output is divided in *blocks*, each defining variables in order to access the Monte Carlo truth or to reconstruct an experimental-like event. The first block shows the information about the passage of a particle between different regions (air, converter fibres, calorimeter pixels etc.). The second block contains the physical properties and the main information about the dynamics of each particle. The last blocks contain variables equivalent to experimental ones, such as particle energy releases in active regions. Some of the reported data, such as the particle id that generated the energy release, are not experimentally accessible. These variables cannot be used to develop an algorithm to analyse the experimental data but are useful to verify its performance.

Data type	**Variable name**	**Variable description**
Int	ncross	number of event crossings
Int	idcross[ncross]	particle id code
Int	nregcross[ncross]	region where the particle enters
Int	nregold[ncross]	region from which the particle comes out
Double	xcross[ncross]	crossing position (X coordinate)
Double	ycross[ncross]	crossing position (Y coordinate)
Double	zcross[ncross]	crossing position (Z coordinate)
Double	pxcross[ncross]	particle momentum (X component) at crossing
Double	pycross[ncross]	particle momentum (Y component) at crossing
Double	pzcross[ncross]	particle momentum (Z component) at crossing
Double	tcross[ncross]	time of crossing

Table A.2: FLUKA output variables related to the passage of a particle from a region to another. [n] indicates an array of n values.

Data type	Variable name	Variable description
Int	nump	number of particles in the event
Int	idpa [nump]	particle parent id code
Int	igen [nump]	interaction in which the particle is generated
Int	icha [nump]	particle charge
Int	numreg [nump]	region in which the particle is generated
Int	iba [nump]	particle barionic number
Int	idead [nump]	interaction in which the particle dies
Int	jpa [nump]	FLUKA code for the particle type
Double	vxi [nump]	generation point (X coordinate)
Double	vyi [nump]	generation point (Y coordinate)
Double	vzi [nump]	generation point (Z coordinate)
Double	vxf [nump]	death point (X coordinate)
Double	vyf [nump]	death point (Y coordinate)
Double	vzf [nump]	death point (Z coordinate)
Double	px [nump]	momentum (X component) at the generation point
Double	py [nump]	momentum (Y component) at the generation point
Double	pz [nump]	momentum (Z component) at the generation point
Double	pxf [nump]	momentum (X component) at the death point
Double	pyf [nump]	momentum (Y component) at the death point
Double	pzf [nump]	momentum (Z component) at the death point
Double	amass [nump]	particle mass
Double	tempo [nump]	generation time of the particle
Double	tof [nump]	time of flight of the particle
Double	trlen [nump]	length of the particle path

Table A.1: Variables of FLUKA output related to the particles produced in the event considered. [n] indicates an array of n values.

Data type	Variable name	Variable description
Int	ncountconv	number of hits in the converter
Int	idconv[ncountconv]	id of the particle that generated the hit
Int	numconv[ncountconv]	number of the fiber in which the energy release occured
Double	xinconv[ncountconv]	entry point into the fiber (X coordinate)
Double	yinconv[ncountconv]	entry point into the fiber (Y coordinate)
Double	zinconv[ncountconv]	entry point into the fiber (Z coordinate)
Double	pxinconv[ncountconv]	particle momentum (X component) at entry into the fiber
Double	pyinconv[ncountconv]	particle momentum (Y component) at entry into the fiber
Double	pzinconv[ncountconv]	particle momentum (Z component) at entry into the fiber
Double	timconv[ncountconv]	time of entry
Double	xoutconv[ncountconv]	exit point from the fiber (Y coordinate)
Double	youtconv[ncountconv]	exit point from the fiber (Z coordinate)
Double	zoutconv[ncountconv]	exit point from the fiber (X coordinate)
Double	pxoutconv[ncountconv]	particle momentum (X component) at exit from the fiber
Double	pyoutconv[ncountconv]	particle momentum (Y component) at exit from the fiber
Double	pzoutconv[ncountconv]	particle momentum (Z component) at exit from the fiber
Double	deconv[ncountconv]	particle energy release in the fiber

Table A.3: FLUKA output variables related to an energy release in the converter. [n] indicates an array of n values.

Data type	Variable name	Variable description
Int	ncountalp	number of hits in the ALPIDEs
Int	idalp[ncountalp]	id of the particle that generated the hit
Int	planealp[ncountalp]	ALPIDE plane in which the energy release occured
Int	rowalp[ncountalp]	pixel row in which the energy release occured
Int	colalp[ncountalp]	pixel column in which the energy release occured
Double	xinalp[ncountalp]	entry point into the pixel (X coordinate)
Double	yinalp[ncountalp]	entry point into the pixel (Y coordinate)
Double	zinalp[ncountalp]	entry point into the pixel (Z coordinate)
Double	pxinalp[ncountalp]	particle momentum (X component) at entry into the pixel
Double	pyinalp[ncountalp]	particle momentum (Y component) at entry into the pixel
Double	pzinalp[ncountalp]	particle momentum (Z component) at entry into the pixel
Double	timalp[ncountalp]	time of entry
Double	xoutalp[ncountalp]	exit point from the pixel (Y coordinate)
Double	youtalp[ncountalp]	exit point from the pixel (Z coordinate)
Double	zoutalp[ncountalp]	exit point from the pixel (X coordinate)
Double	pxoutalp[ncountalp]	particle momentum (X component) at exit from the pixel
Double	pyoutalp[ncountalp]	particle momentum (Y component) at exit from the pixel
Double	pzoutalp[ncountalp]	particle momentum (Z component) at exit from the pixel
Double	dealp[ncountalp]	particle energy release in the pixel

Table A.4: FLUKA output variables related to an energy release in the tracker. [n] indicates an array of n values.

Data type	Variable name	Variable description
Int	ncountcalo	number of hits in the converter
Int	idcalo[ncountcalo]	id of the particle that generated the hit
Int	rowcalo[ncountcalo]	pixel row in which the energy release occured
Int	colcalo[ncountcalo]	pixel column in which the energy release occured
Double	xincalo[ncountcalo]	entry point into the pixel (X coordinate)
Double	yincalo[ncountcalo]	entry point into the pixel (Y coordinate)
Double	zincalo[ncountcalo]	entry point into the pixel (Z coordinate)
Double	pxincalo[ncountcalo]	particle momentum (X component) at entry into the pixel
Double	pyincalo[ncountcalo]	particle momentum (Y component) at entry into the pixel
Double	pzincalo[ncountcalo]	particle momentum (Z component) at entry into the pixel
Double	timcalo[ncountcalo]	time of entry
Double	xoutcalo[ncountcalo]	exit point from the pixel (Y coordinate)
Double	youtcalo[ncountcalo]	exit point from the pixel (Z coordinate)
Double	zoutcalo[ncountcalo]	exit point from the pixel (X coordinate)
Double	pxoutcalo[ncountcalo]	particle momentum (X component) at exit from the pixel
Double	pyoutcalo[ncountcalo]	particle momentum (Y component) at exit from the pixel
Double	pzoutcalo[ncountcalo]	particle momentum (Z component) at exit from the pixel
Double	decalo[ncountcalo]	particle energy release in the pixel

Table A.5: FLUKA output variables related to an energy release in the calorimeter. [n] indicates an array of n values.

Bibliography

[1] Stewart. "World Cancer Report 2014. International Agency for Research on Cancer". In: 3 (2014).

[2] Patera *et al.* "Nuclear interactions and medicine". In: *The European Physical Journal Plus* 134.1 (2019).

[3] Wilson. "Radiological use of fast protons". In: *Radiology* 47.5 (1946).

[4] Jermann. "Particle therapy statistics in 2014". In: *International Journal of Particle Therapy* 2.1 (2015).

[5] PTCOG. *Particle therapy facilities under construction*. 2019. URL: http://www.ptcog.ch (visited on 03/18/2020).

[6] PTCOG. *Particle therapy facilities in clinical operation*. 2020. URL: http://www.ptcog.ch (visited on 03/18/2020).

[7] Leo. *Techniques for nuclear and particle physics experiments: a how-to approach*. Springer Science & Business Media, 2012.

[8] NIST. *Stopping-power and range tables for proton*. URL: https://physics.nist.gov/PhysRefData/Star/Text/PSTAR.html (visited on 03/18/2020).

[9] Testa. "Charged particle therapy, ion range verification, prompt radiation". PhD thesis. 2010.

[10] Schardt *et al.* "Heavy-ion tumor therapy: Physical and radiobiological benefits". In: *Reviews of modern physics* 82.1 (2010).

[11] Terasawa *et al.* "Systematic review: charged-particle radiation therapy for cancer". In: *Annals of internal medicine* 151.8 (2009).

[12] Schardt *et al.* "Nuclear fragmentation of high-energy heavy-ion beams in water". In: *Advances in Space Research* 17.2 (1996).

[13] Gunzert *et al.* "Secondary beam fragments produced by 200 MeV/u 12C ions in water and their dose contributions in carbon ion radiotherapy". In: *New journal of physics* 10.7 (2008).

[14] Amaldi *et al.* "Radiotherapy with beams of carbon ions". In: *Reports on progress in physics* 68.8 (2005), p. 1861.

[15] Hall and Amato. *Radiobiology for the Radiologist*. Vol. 6. Lippincott Williams & Wilkins, 2006.

[16] Scholz *et al.* "Effects of ion radiation on cells and tissues". In: *Radiation effects on polymers for biological use*. Springer, 2003.

[17] Karger. "RBE and related modeling in carbon-ion therapy". In: *Physics in Medicine & Biology* 63.1 (2017).

[18] Raju. "Proton radiobiology, radiosurgery and radiotherapy". In: *International journal of radiation biology* 67.3 (1995).

[19] Krimmer *et al.* "Prompt-gamma monitoring in hadrontherapy: A review". In: *Nuclear Instruments and Methods in Physics Research Section A* 878 (2018).

[20] Schwarz. "Treatment planning in proton therapy". In: *The European Physical Journal Plus* 126.7 (2011).

[21] H. Paganetti. "Range uncertainties in proton therapy and the role of Monte Carlo simulations". In: *Physics in Medicine & Biology* 57.11 (2012).

[22] G.Pausch *et al.* "Detection systems for range monitoring in proton therapy: Needs and challenges". In: *Nuclear Instruments and Methods in Physics Research A* 954 (2018).

[23] Llacer *et al.* "An imaging instrument for positron emitting heavy ion beam injection". In: *IEEE Transactions on Nuclear Science* 26.1 (1979).

[24] K. Parodi. "On-and off-line monitoring of ion beam treatment". In: *Nuclear Instruments and Methods in Physics Research Section A* 809 (2016).

[25] K. Parodi. "PET monitoring of hadrontherapy". In: *Nuclear Medicine Review* 15.C (2012), pp. 37–42.

[26] Ferrero *et al.* "Online proton therapy monitoring: clinical test of a Silicon-photodetector-based in-beam PET". In: *Scientific reports* 8.1 (2018).

[27] Enghardt *et al.* "Charged hadron tumour therapy monitoring by means of PET". In: *Nuclear Instruments and Methods in Physics Research Section A* 525.1-2 (2004).

[28] Pinto *et al.* "Absolute prompt-gamma yield measurements for ion beam therapy monitoring". In: *Physics in Medicine & Biology* 60.2 (2014).

[29] Battistoni *et al.* "The FLUKA code: an accurate simulation tool for particle therapy". In: *Frontiers in oncology* 6 (2016).

[30] Verburg *et al.* "Energy-and time-resolved detection of prompt gamma-rays for proton range verification". In: *Physics in Medicine & Biology* 58.20 (2013).

[31] Smeets *et al.* "Prompt gamma imaging with a slit camera for real-time range control in proton therapy". In: *Physics in Medicine & Biology* 57.11 (2012).

[32] Park *et al.* "Comparison of knife-edge and multi-slit camera for proton beam range verification by Monte Carlo simulation". In: *Nuclear Engineering and Technology* 51.2 (2019).

[33] Thirolf *et al.* "Development of a Compton camera for online range monitoring of laser-accelerated proton beams via prompt-gamma detection". In: vol. 66. EDP Sciences. 2014.

[34] Werner *et al.* "Processing of prompt gamma-ray timing data for proton range measurements at a clinical beam delivery". In: *Physics in Medicine & Biology* 64.10 (2019).

[35] Hueso-Gonz *et al.* "A full-scale clinical prototype for proton range verification using prompt gamma-ray spectroscopy". In: *Physics in Medicine & Biology* 63.18 (2018).

[36] Krimmer *et al.* "A cost-effective monitoring technique in particle therapy via uncollimated prompt gamma peak integration". In: *Applied Physics Letters* 110.15 (2017).

[37] Piersanti *et al.* "Measurement of charged particle yields from PMMA irradiated by a 220 MeV/u 12C beam". In: *Physics in Medicine & Biology* 59.7 (2014).

[38] Muraro *et al.* "Monitoring of hadrontherapy treatments by means of charged particle detection". In: *Frontiers in oncology* 6 (2016).

[39] Gwosch *et al.* "Non-invasive monitoring of therapeutic carbon ion beams in a homogeneous phantom by tracking of secondary ions". In: *Physics in Medicine & Biology* 58.11 (2013).

[40] Traini *et al.* "Review and performance of the Dose Profiler, a particle therapy treatments online monitor". In: *Physica Medica* 65 (2019).

[41] Kanbach *et al.* "The project EGRET (energetic gamma-ray experiment telescope) on NASA's Gamma-Ray Observatory GRO". In: *Space Science Reviews* 49.1-2 (1989).

[42] Wu *et al.* "PANGU (PAir-productioN Gamma-ray Unit): A High Resolution Gamma-ray Space Telescope)". In: *PoS* (2015).

[43] Krane *et al. Introductory nuclear physics*. 1987.

[44] Blackett *et al.* "Some photographs of the tracks of penetrating radiation". In: *Proceedings of the Royal Society of London. Series A, Containing Papers of a Mathematical and Physical Character* 139.839 (1933).

[45] Motz *et al.* "Pair production by photons". In: *Reviews of Modern Physics* 41.4 (1969).

[46] Barò *et al.* "Analytical cross sections for Monte Carlo simulation of photon transport". In: *Radiation physics and chemistry* 44.5 (1994).

[47] Salvat *et al.* "PENELOPE-2006: A code system for Monte Carlo simulation of electron and photon transport". In: *Workshop proceedings*. Vol. 4. 6222. 2006.

[48] Glenn F Knoll. *Radiation detection and measurement*. John Wiley & Sons, 2010.

[49] Rinella *et al.* "The ALPIDE pixel sensor chip for the upgrade of the ALICE Inner Tracking System". In: *Nuclear Instruments and Methods in Physics Research Section A: Accelerators, Spectrometers, Detectors and Associated Equipment* 845 (2017).

[50] Eljentechnology. *Plastic Scintillators*. 2020. URL: https://eljentechnology.com/products/plastic-scintillators/ej-200-ej-204-ej-208-ej-212 (visited on 03/18/2020).

[51] Ferrari *et al.* "FLUKA: a multi-particle transport code CERN-2005-10". In: *INFN/TC* 5 (2005).

[52] Bohlen *et al.* "The FLUKA code: developments and challenges for high energy and medical applications". In: *Nuclear data sheets* 120 (2014).

[53] Mattei *et al.* "Scintillating Fiber Devices for Particle Therapy Applications". In: *IEEE Transactions on Nuclear Science* 65.8 (2018).

[54] Janssen. "93: Robustness of range prediction in proton therapy using prompt gamma emission". In: *Radiotherapy and Oncology* 110 (2014).

[55] Saint-Gobain. URL: https://www.crystals.saint-gobain.com/products/prelude-420-LYSO (visited on 03/18/2020).